RESEARCH   **Open Access**

Carotid artery vascular stenosis causes the blood-CSF barrier damage and neuroinflammation

Lin Lin[1,2,3], Yang Chen[2,3], Kai He[2,3], Shamseldin Metwally[2,3], Roshani Jha[2], Okan Capuk[2,3], Mohammad Iqbal H. Bhuiyan[5], Gazal Singh[4], Guodong Cao[2,6], Yan Yin[1*] and Dandan Sun[2,3,6*]

Abstract

Background The choroid plexus (ChP) helps maintain the homeostasis of the brain by forming the blood-CSF barrier via tight junctions (TJ) at the choroid plexus epithelial cells, and subsequently preventing neuroinflammation by restricting immune cells infiltration into the central nervous system. However, whether chronic cerebral hypoperfusion causes ChP structural damage and blood-CSF barrier impairment remains understudied.

Methods The bilateral carotid stenosis (BCAS) model in adult male C57BL/6 J mice was used to induce cerebral hypoperfusion, a model for vascular contributions to cognitive impairment and dementia (VCID). BCAS-mediated changes of the blood-CSF barrier TJ proteins, apical secretory Na^+-K^+-Cl^- cotransporter isoform 1 (NKCC1) protein and regulatory serine-threonine kinases SPAK, and brain infiltration of myeloid-derived immune cells were assessed.

Results BCAS triggered dynamic changes of TJ proteins (claudin 1, claudin 5) accompanied with stimulation of SPAK-NKCC1 complex and NF-κB in the ChP epithelial cells. These changes impacted the integrity of the blood-CSF barrier, as evidenced by ChP infiltration of macrophages/microglia, neutrophils and T cells. Importantly, pharmacological blockade of SPAK with its potent inhibitor ZT1a in BCAS mice attenuated brain immune cell infiltration and improved cognitive neurological function.

Conclusions BCAS causes chronic ChP blood-CSF damage and immune cell infiltration. Our study sheds light on the SPAK-NKCC1 complex as a therapeutic target in neuroinflammation.

Keywords Chronic cerebral hypoperfusion, SPAK-NKCC1 complex, Tight junction damage, The blood-CSF barrier, Vascular dementia

*Correspondence:
Yan Yin
yanyin1208@126.com
Dandan Sun
sund@upmc.edu
[1] Department of Neurology, The Second Hospital of Dalian Medical University, Dalian 116027, Liaoning, China
[2] Department of Neurology, University of Pittsburgh Medical Center, 7016 Biomedical Science Tower 3, 3501 Fifth Ave., Pittsburgh, PA 15213, USA
[3] Pittsburgh Institute for Neurodegenerative Disorders, University of Pittsburgh, Pittsburgh, PA, USA
[4] Biomedical Masters Program, School of Medicine, University of Pittsburgh, Pittsburgh, PA, USA
[5] The University of Texas at El Paso, El Paso, TX, USA
[6] Research Service, Veterans Affairs Pittsburgh Health Care System, Pittsburgh, PA, USA

Lin *et al. Journal of Neuroinflammation* (2024) 21:220

Page 2 of 23

Background

Vascular contributions to cognitive impairment and dementia (VCID) have been identified as an important pathologic process in the initiation and progression of vascular dementia and Alzheimer's disease (AD), which together account for approximately 60–80% of dementia worldwide [1, 2]. Chronic cerebral hypoperfusion resulting from either large or small cerebral vessel diseases (such as carotid atherosclerosis or arteriosclerosis) causes cognitive impairment and dementia [1, 3]. Characteristic pathology of VCID includes white matter lesions, cerebral atrophy, gliosis, and endothelial damage [1, 4]. Neuroinflammation has been determined as one of principal contributors to these pathological alterations [1, 5, 6]. The choroid plexus (ChP), located in the brain ventricles, is considered a key entry point for immune cells into the central nervous system (CNS) and acts as a regulatory barrier for immune cells between the peripheral and CNS [7–9]. The ChP consists of highly vascularized stroma surrounded by a continuous layer of epithelial cells held together by tight junctions (TJs) as the blood-CSF barrier, that allows for a tightly regulated bidirectional immunosurveillance system in which immune cells can traffic through the ChP into the CNS, but also vice versa [7, 8]. In animal models of AD, β-amyloid can induce an upregulation of inflammatory cytokines (IL-1, IL-6, TNF-α) and matrix metalloproteinases (MMP-3, MMP-9) and downregulation of TJs (ZO-1, claudin-1, claudin-5, occludin), leading to an early disruption of the blood-CSF barrier and neuroinflammation [10] [11] and progression of the disease [11]. However, whether chronic cerebral hypoperfusion causes impaired blood-CSF barrier structure and integrity and neuroinflammation remains unknown. Moreover, the ChP epithelial serine-proline-alanine kinase (SPAK) plays a multifaceted role by mediating immune cell signaling and modulating the secretion of CSF via phosphorylation and activation of the apical secretory ion transporter Na–K–Cl Cotransporter (NKCC1) [12, 13]. This regulatory function is facilitated through the interaction of SPAK with the upstream tumor necrosis factor-alpha (TNF-α) receptor and the downstream ion transporter NKCC1, thus establishing SPAK as a critical regulatory protein in the homeostasis of CSF [12, 13]. Post-infectious hydrocephalus and post-hemorrhagic hydrocephalus trigger activation of SPAK-NKCC1 protein complex in the ChP [14]. Activation of NF-kB also plays an important role in pathological activation of NKCC1 in ChP epithelial cells [12, 13, 15] and other brain cells (astrocytes, microglial, neurons) [16–18]. Whether the chronic hypoperfusion induces any changes in ChP SPAK-NKCC1 cascade also remains unknown.

In this study, using mouse bilateral carotid stenosis (BCAS)-induced VCID model, we report that BCAS led to chronic reduction of cerebral blood flow (CBF) by 20–40%. At 4–8 weeks (weeks) post-BCAS, the ChP epithelial cells displayed dynamic changes of TJ proteins and sustained upregulation of NKCC1 and dynamic changes of SPAK (total and phosphorylated). These changes were accompanied with the infiltration of myeloid-derived immune cells in the ChP and cerebral brain tissues. Importantly, post-BCAS pharmacological blockade of SPAK with the inhibitor ZT-1a attenuated the above pathological ChP damages and improved cognitive neurological function in mice. Our study sheds light on the SPAK-NKCC1 complex as a therapeutic target in neuroinflammation in VCID.

Materials and methods

Materials

Novel SPAK inhibitor ZT-1a was developed as described before [19]. Rabbit anti-pSPAK/pOSR1 (pSer383 SPAK/pSer325 OSR1), rabbit anti-SPAK/OSR1 were developed by Dr. Yang at Taiwan National University [20, 21], rabbit anti-SPAK was from Cell Signaling Technology (Cat# 2281S, USA), and rabbit anti-pSPAK was from EMD Millipore (Cat# 07-2273, USA). Rabbit anti-NKCC1 (S1c12a2) was from BiCelln (Cat#20302, USA), mouse monoclonal anti-NKCC (T4) was from the Developmental Studies Hybridoma Bank (Cat# T4, Iowa City, IA), and rabbit anti-pNKCC1 was from EMD Millipore Novel (Cat# ABS1004, USA). Rabbit anti-ZO-1 was from Invitrogen (Cat# 40-2200, USA), rabbit anti-claudin-1 was from Invitrogen (Cat# 51-9000, USA), mouse anti-claudin-5 was from Invitrogen (Cat# 35-2500, USA), and mouse anti-cytokeratin was from Sigma (Cat# C2562, USA). Goat anti-rabbit 546 (Cat# A11035, USA) and goat-anti-rabbit 488 (Cat# A11008, USA) were from Thermo Fisher, and rabbit anti-GAPDH was from Cell Signaling (Cat# 2118S, USA). RIPA buffer (Cat# 89901, USA), protease inhibitor cocktail (Cat# 78438, USA), the mixture of BCA Reagent A solution (Cat#23228, USA) and BCA Reagent B solution (Cat#23224, USA) were from Thermo Fisher Scientific. The phosphatase inhibitor cocktail was from Roche (Cat# 04906837001, UAS). All are as described in Supplemental Table -1.

Animals

All animal studies were approved by the University of Pittsburgh Medical Center Institutional Animal Care and Use Committee, which adhere to the National Institutes of Health Guide for the Care and Use of Laboratory Animals and reported in accordance with the Animal Research: Reporting In Vivo Experiments (ARRIVE) guidelines 2.0 [22]. The C57Bl/6 J strain mice used in

Lin *et al. Journal of Neuroinflammation*   (2024) 21:220

Page 3 of 23

the study were purchased from Jackson laboratories (Bar Harbor, ME). Mice were housed in a temperature-controlled room on a 12-h light/12-h dark cycle with standard mouse diet and water ad libitum. All efforts were made to minimize the number of animals used.

Bilateral common carotid artery stenosis (BCAS) model

A bilateral common carotid artery stenosis (BCAS) model in C57BL/6 J mice (male and female, 12–16 weeks old, weighing 25–35 g) was induced to simulate vascular cognitive impairment and dementia (VCID). For BCAS surgery, mice were anesthetized with 3% isoflurane in a mixture of N_2O and O_2 (3:2) and maintained with 1.5% isoflurane while their body temperature was kept at 36.5 ± 0.5 °C using a heating pad as described before [23]. Mice were placed in a supine position on the surgical table after shaving and disinfecting the neck skin. A 2-cm vertical incision was made in the midline of the neck at 0.5 cm above the sternum. The subcutaneous tissue was bluntly dissected under a surgical microscope to expose the bilateral common carotid arteries. The left common carotid artery was separated from the left vagus nerve and surrounding tissues. Two 7-0 silk sutures were passed through the proximal and distal ends of the left common carotid artery. The artery was gently lifted with the sutures, and a 0.18 mm internal diameter spring wire coil (Sawane Spring Company, Japan) was rotated and wrapped around the left common carotid artery below the carotid bifurcation. The right common carotid artery, vagus nerve, and surrounding tissues were then similarly separated, and the spring wire coil was wrapped around the right common carotid artery. The incision was closed and 50 μL of 0.25% bupivacaine hydrochloride was locally infiltrated for anesthesia. The mice were allowed to recover from anesthesia before being returned to their normal cages for daily food and water intake. Animals in the sham surgery group underwent the same procedure, except that the spring wire coil was not placed on the common carotid arteries. Sham or BCAS mice at 4-, 6-, and 8-week (wk) post-surgery were subjected to either neurological function assessment or biochemical studies.

Cerebral blood flow (CBF) measurement

A two-dimensional laser speckle contrast analysis system (PeriCam PSI High Resolution with PIMSoft, Perimed, Sweden) was used to measure relative changes of cerebral blood flow (rCBF) in the mice. Mice were anesthetized with 3% isoflurane in a mixture of N_2O and O_2 (3:2) and maintained with 1.5% isoflurane as described above. After removing the fur on the scalp and disinfecting the skin, a midline incision was made on the scalp, and the exposed skull surface was washed with sterile physiological saline. The speckle images were captured using a camera placed 10-cm above the skull surface, covering two symmetrical and identical regions of interest (ROI) at each hemisphere including the cerebral frontal cortex and cerebellum. The CBF values were measured at 10–20 min before surgery, 10 min, 3 days, 7 days, 14 days, 28 days and 56 days after Sham or BCAS surgery. The percentage change of rCBF at each time point was calculated by comparing the mean signal intensity with the baseline signal intensity. To avoid potential confounding effects of the isoflurane on CBF, 3% isoflurane for induction and 1.5% isoflurane for maintenance were consistently used for each rCBF measurement. Different n values in the Sham and BCAS groups in Fig. 1C were due to over scheduled experiments and missing data collection for 1–3 mice at day 3 and day 28 post-surgery.

Administration of SPAK inhibitor ZT-1a

BCAS mice were randomly assigned to receive either vehicle (Veh) (100% DMSO, 2 ml/kg body weight/day, n=30) or ZT-1a (5 mg/kg in DMSO body weight/day, n=30) every 2 days via intraperitoneal (i.p.) injection from 14–28 days or 28–56 days post-surgery. For Fig. 3, the stock concentration of ZT-1a was 1.25 mg/ml (dissolved in 100% DMSO) and ZT-1-treated mice received 4 ml/kg DMSO, which is within the tolerable DMSO dose (10 ml/kg) [24]. To reduce DMSO administration for Figs. 4, 5, 6, 7, 8, 9, the ZT-1a stock concentration was increased to 2.5 mg/ml and the ZT-1a-treated mice received 2 ml/kg DMSO every 2 days, which was identical to the vehicle groups.

Neurological behavioral tests

Mice were subject to neurobehavioral tests, including the open field test for anxiety and locomotor activity and the Y-maze spontaneous alternation test and novel spatial recognition (NSR) test for assessing spatial working memory changes. Open field test: Mice were placed in the center of a square apparatus measuring 40 cm in length, width, and height. A camera was placed on top of the box and connected to a behavior tracking software (Fusion) to record the total distance traveled by the mice (in centimeters), vertical activity counts (measured by the number of beam breaks), and time spent at the periphery of the box over a 60-min period. Y-maze spontaneous alternation test: Mice were placed in a Y-shaped transparent arena consisting of three arms, each measuring 33.7 cm in length, 6 cm in width, and 5 cm in height, and allowed to freely explore for 8 min. Behavior tracking software (Noldus Ethovision XT) was used to record the number of entries into each arm (counted as one entry when all four paws of the mouse were inside the arm) and the number of spontaneous alternations (defined as consecutive entries into each of the three arms). Y-Maze
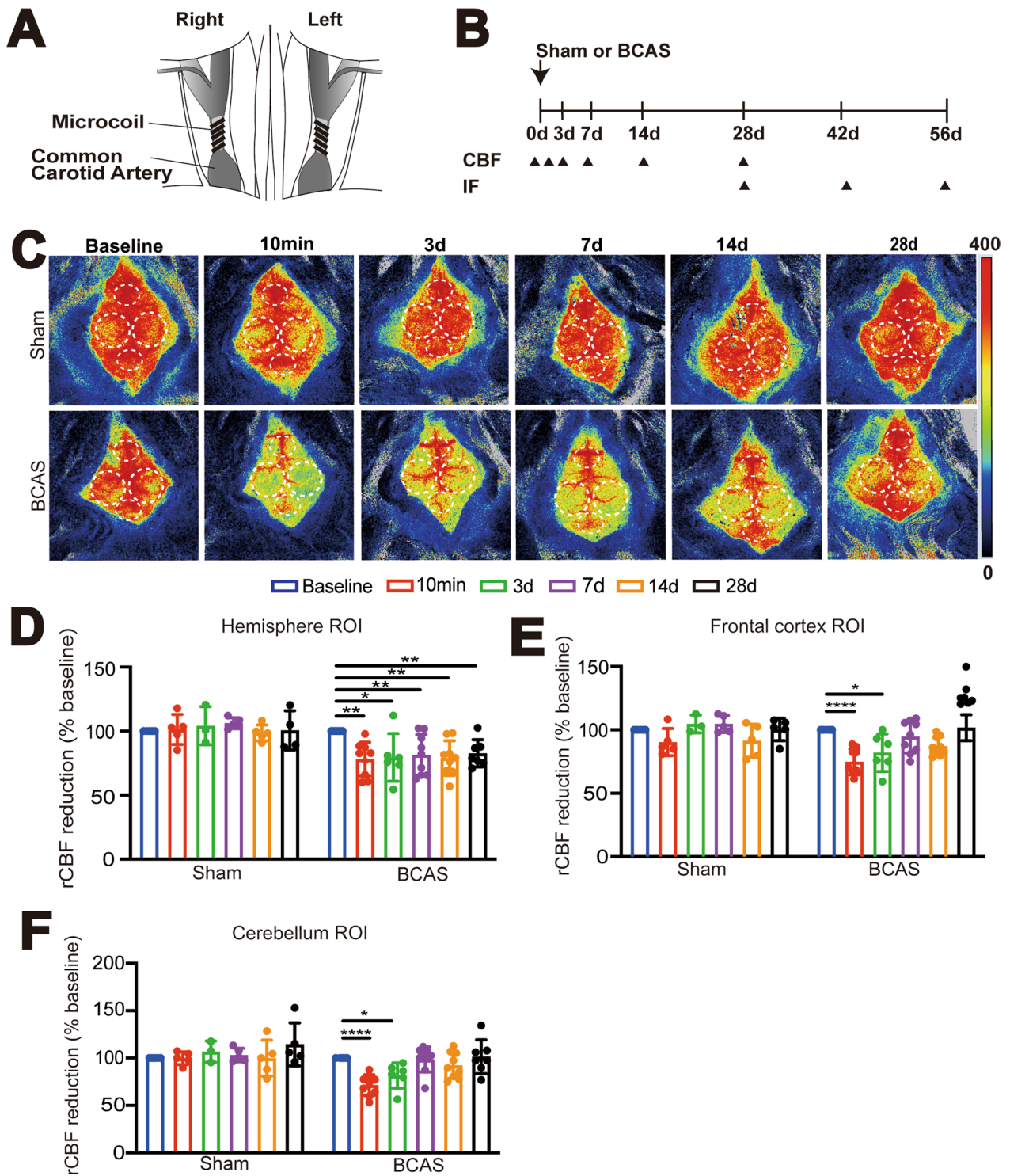
Lin *et al. Journal of Neuroinflammation*   (2024) 21:220

Page 4 of 23

Fig. 1 Bilateral carotid artery stenosis (BCAS) in mice induces sustained cerebral hypoperfusion. **A** Illustration of BCAS model modified from the paper by Ref Eun et al. [28]. **B** Experimental protocol. Mice underwent Sham or BCAS surgery. Arrowheads: indicate the time points at which the cerebral blood flow (CBF) or immunostaining (IF) were performed. **C** Representative periCam PSI images by a two-dimensional laser speckle contrast analysis system (PSI analysis) of regional CBF (rCBF) in male C57/B6J mice before, 10 min, 3 days, 7 days, 14 days, and 28 days after Sham or BCAS surgery. Dashedcircle: region of interest (ROI). **D–F** Quantification analysis of rCBF. Data are expressed as mean ± SD. n = 5–8 per group. *p < 0.05, **p < 0.01 vs. Sham. One Sample t-test

Lin *et al. Journal of Neuroinflammation* (2024) 21:220

Page 5 of 23

novel spatial recognition (NSR) test: Mice were placed in the Y-shaped transparent arena with three arms. The test was conducted in two phases: the familiarization phase and the test phase. Familiarization Phase: Mice were allowed to explore two arms of the Y-maze for 10 min, with one arm blocked off. After the familiarization period, mice were returned to their home cage. Test Phase: The blocked arm was opened, and the mouse was returned to the Y-maze. The mouse was allowed to explore all three arms freely for 5 min. And behavior tracking software (Noldus Ethovision XT) was used to record the number of entries into each arm (counted as one entry when all four paws of the mouse were inside the arm) and the time spent in each arm. To assess the mouse's preference for the novel arm, the Recognition Index was calculated as a ratio of Time spent in the novel arm / Total time spent in all three arms.

Immunofluorescent staining and image analysis

Mice were anesthetized with 3% isoflurane and transracially perfused with physiological saline and 4% paraformaldehyde. Brain tissue was stored in 4% paraformaldehyde for 24 h and then transferred to a 30% sucrose solution for cryopreservation. Coronal brain slices (16 μm or 25 μm thickness) containing lateral ventricle ChP (LVCP, located at − 0.5 to − 1.0 mm from the bregma approximately, 20–30 slices) were selected from each mouse and then blocked with blocking solution (10% normal goat serum (NGS) and 0.5% Triton X-100) at room temperature (RT) for 1 h, followed by incubation with primary antibodies overnight at 4 °C. On the second day, the brain slices were washed with PBS and incubated with corresponding secondary antibodies at RT for 1 h. After three washes, the cell nuclei were stained with DAPI (1:1000, dissolved in blocking solution) and the slices were then mounted with Vectashield antifade mounting medium (Vector Laboratories, Burlingame, CA). Negative controls were performed in brain slices stained only with secondary antibodies without primary antibodies (Supplemental Figure S2).

Fluorescent images of LVCP were acquired using Nikon A1R Confocal Microscope system, and a 40×oil immersion objective. Three regions of interest (ROI 1–3) were selected from each side of the LVCP (as illustrated in Fig. 2A), totaling 6 ROIs/mouse brain. The same digital imaging acquisition parameters were used throughout the study, and fluorescent images were analyzed by a blinded observer using Image J software for quantitative analysis. The mean fluorescence intensity of these 6 ROIs per brain (ROI 1, 2, and 3 from each side) was used for quantification of the mean values, represented as a single point on the graph for each brain. Therefore, all points on the graphs represented independent values from different mice.

Imaris 3D reconstruction of the ChP epithelial cells

Z-stacks analysis and 3D cell reconstruction of the ChP epithelial cells were executed using Imaris 10.0.1 program (Andor Technology, Belfast, UK). Three different surface analyses with Channel 2—FITC, Channel 3—Cy3, and DAPI as the source channels were done to reconstruct immunostaining images of claudin-1, claudin-5, E-cadherin and the DAPI nuclei as 3D structures of the ChP epithelial cells, respectively. We used the built-in "XTension" called "Set angle of the camera", which enables to set specific values for the angle, elevation, and azimuth of the camera. A similar value for the angle was used when taking representative images of the ChP epithelial cells. Identical surface detail value and thresholding were applied in the analysis of each channel respectively. To quantify nuclear pNF-kB immunosignal, the surface tool was used to reconstruct DAPI and uniform XY diameter was applied across all stacked images. Using the spots tool, a filter was applied to remove all spots outside the reconstructed DAPI surface, retaining only the reconstructed pNF-kB immunoreactive spots within the reconstructed structures. Subsequently, the 'Total Number of Spots' divided by the "Total Number of Surfaces" was plotted for each stacked image for quantification of nuclear pNF-kB immunosignal density.

ChP tissue preparation and immunoblotting

Mice were euthanized with CO_2 and transcardially perfused with ice-cold PBS as described before [25]. LVCP

(See figure on next page.)

Fig. 2 BCAS induces dynamic changes of ChP SPAK-NKCC1 complex protein expression. **A** Representative images of left and right LVCP of Sham brains stained for epithelial cytoskeletal cytokeratin protein. Dashed box: ROI for data quantification. **B** Representative images of immunofluorescent staining of SPAK and NKCC1 proteins in LVCP of Sham or BCAS mice at 4, 6, or 8 weeks after surgery. Arrowheads: ROI of apical membrane SPAK or NKCC1 protein expression. Arrows: BCAS-induced changes of SPAK and NKCC1 protein. **C** Quantification analysis of SPAK and NKCC1 immunofluorescence intensity in each group. Data are expressed as mean ± SD. n = 4 mouse brains. *p < 0.05, **p < 0.01, ***p < 0.001. One Sample t-test. Unpaired t-test. **D** Representative immunofluorescent staining images of phosphorylated SPAK (pSPAK), and NKCC1 protein (pNKCC1) in LVCP. Arrowheads: apical membrane expression of pSPAK or pNKCC1 protein. Arrows: BCAS-induced changes of pSPAK and pNKCC1 protein expression. **E** Quantification analysis of pSPAK and pNKCC1 immunofluorescence intensity in each group. Data are expressed as mean ± SD. n = 4 mouse brains. *p < 0.05. One Sample t-test. Unpaired t-test
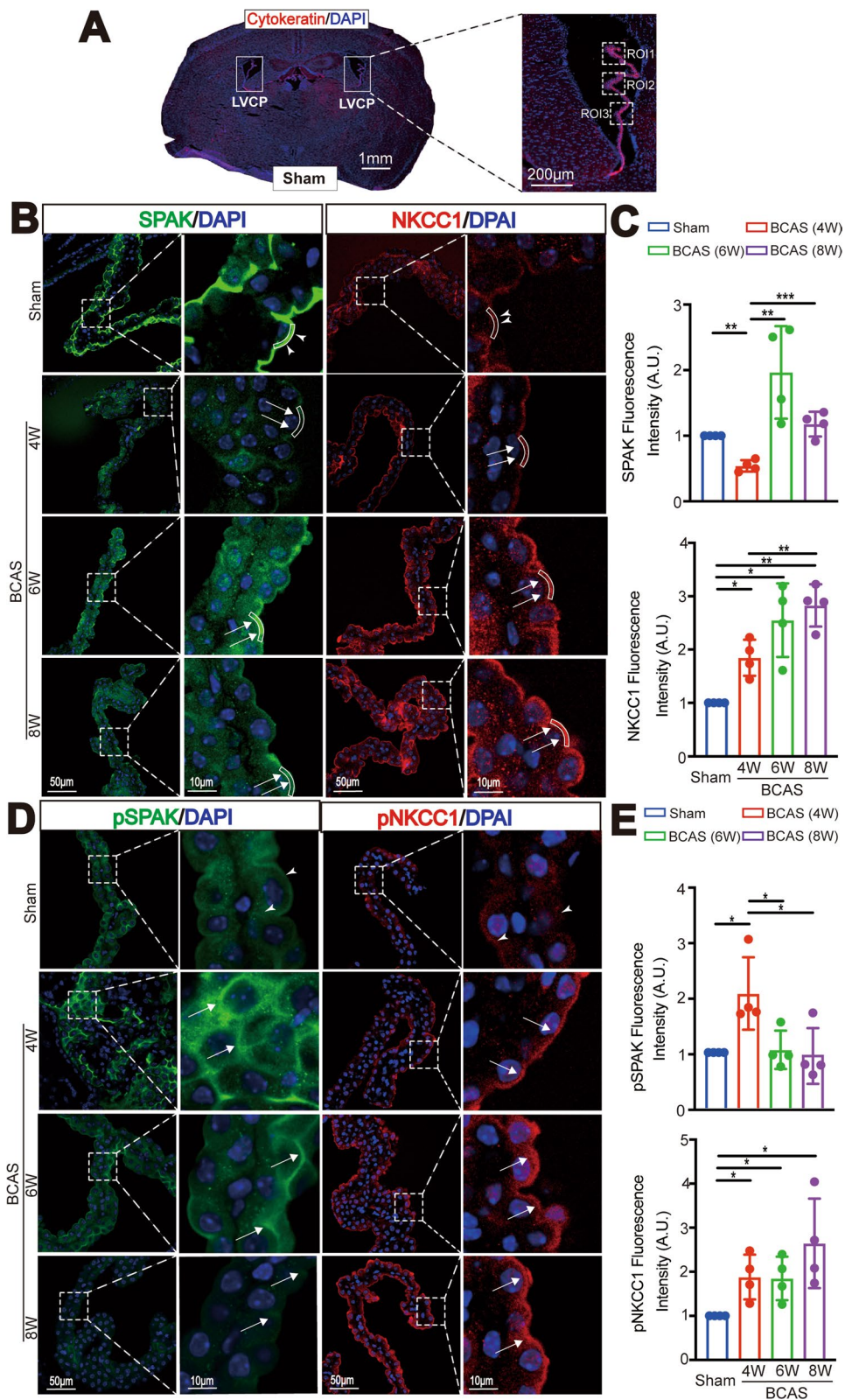
Lin *et al. Journal of Neuroinflammation*   (2024) 21:220

Page 6 of 23

Fig. 2 (See legend on previous page.)

Lin *et al. Journal of Neuroinflammation*   (2024) 21:220

Page 7 of 23

was isolated under a microscope and placed in 1.5 ml tubes with ice-cold PBS. LVCP were incubated in RIPA buffer containing a phosphatase inhibitor cocktail and 2 mM protease inhibitor cocktail. The samples were then centrifuged at 14,000 rpm for 10 min (4 ℃). Supernatant was pipetted into a 0.5 ml tube and stored at − 80 ℃. The protein concentration was determined by the BCA method (with a mixture of BCA Reagent A solution and BCA Reagent B solution (at 50:1). Protein samples (20–30 μg) were boiled for 5 min in sample buffer at 95 ℃, separated by 4–15% SDS-PAGE, and transferred onto a nitrocellulose membrane. The membrane was blocked with 1% BSA in PBS-T at RT for 1 h, and then incubated with the appropriate primary antibodies overnight at 4 ℃. The membrane was washed with PBS-T and incubated with IRDye® horseradish peroxidase-conjugated secondary antibodies (1:20,000) at RT for 1 h. Protein bands were visualized directly using Odyssey® Imaging Systems. The density of protein bands were analyzed using Image J with actin expression as a loading control.

ELISA measurement of albumin in CSF and serum

Blood sample (0.5 ml) from each mouse was obtained by cardiac puncture from isoflurane anesthetized mice and left in the test tube at RT for 30 min for clotting. After centrifuge at 1500×g (4 ℃) for 15 min, the serum layer was collected and stored at − 80 ℃. To collect cerebrospinal fluid (CSF) from the cisterna magna, mouse's head was positioned at a 135° angle from the body using a stereotaxic frame. A capillary was punctured into the cisterna magna and 4–8 μL CSF was withdrawn. After centrifugation at 1500×g (4 ℃) for 10 min, the CSF supernatant was obtained and stored at − 80 ℃. Albumin concentrations in CSF and sera were measured by using RayBio mouse albumin ELISA kit (RayBiotech, Catalog# ELM-Albumin) with the dilution of CSF (1:2000) and serum (1: 1.5×10^6). The assay was performed according to the manufacturer's instructions. The ratio values of CSF Albumin/Serum Albumin were calculated for the assessment of blood-CSF brain barrier permeability changes.

Flow cytometric analysis of immune cells in cerebral hemisphere and ChP

Animals were deeply anesthetized with 5% isoflurane and transcardially perfused with ice-cold PBS [15] in which the CSF was removed during the myocardial perfusion and brain harvesting. Cerebral hemisphere tissues (including cortex, striatum, and periventricular surrounding tissues) and the LVCP were harvested, respectively. The inflammatory cells infiltrated in the periventricular surrounding tissues have been included in the cerebral hemisphere tissue data but not in the LVCP

data collection. Bilateral LVCP were isolated and enzymatically digested in collagenase type IV (400 U/ml in PBS, 45 min, 37 ℃), and then triturated several times to obtain single cell suspension using a pipette as described before [26]. In addition, bilateral cerebral hemispheric tissues were collected and cut into small pieces and dissociated into a single cell suspension by gentle physical disruption and enzymatic digestion using a tissue dissociation kit according to manufacturer's instructions (Miltenyi Biotech Inc, Bergisch Gladbach, Germany). The single cell suspension sample of cerebral hemispheric tissues was centrifuged through 30/70 Percoll (GE Healthcare, Little Chalfont, UK) gradient solution at 500 g for 30 min to remove myelin. Brain cells were collected from the middle layer and washed twice with HBSS containing 1% fetal bovine serum (FBS) [25]. Both cerebral hemispheric tissues and ChP samples were stained with a mix of antibodies (Supplemental Tabel 1) for 20 min at 4 ℃ in the dark. Data were acquired using an LSRFortessa flow cytometer (BD Biosciences, USA) equipped with FACS Diva software, and a minimum of 20,000 events were recorded for each ChP sample, while hemispheric samples were documented with 50,000 to 100,000 events. Data were analyzed using the Flow Jo software (BD Biosciences, USA) [15] and gating plots were shown in Supplemental Figure S6 and S7.

Statistical analysis

A total of 140 mice were used in this study, including 124 males and 16 females, and all data were included except 5 mice which died during surgery or drug injection. Data were presented as mean and standard deviation (SD) if data was normally distributed. GraphPad Prism software was used for statistical analyses (GraphPad Software, Inc., CA, USA). Researchers blinded to the experimental group assignments evaluated the experimental data. Statistical significance was determined by one sample t test, unpaired t test, one-way analysis of variance (ANOVA) or two-way ANOVA as indicated. When the Sham control group or baseline level group was set to a hypothetical value such as 1 or 100, One Sample t-test method was used to compare with other experimental groups against the hypothetical value for assessment. Unpaired t-test was used to compare data between experimental groups. A p value < 0.05 was considered statistically significant.

Results

BCAS induces chronic reduction in rCBF

Sham control (Ctrl) or BCAS surgeries were performed in C57BL/6 J male mice (Fig. 1A, B) and BCAS-induced cerebral hypoperfusion was assessed by PeriCam laser speckle contrast analysis. We measured the rCBF in the cerebral hemisphere including cerebral frontal cortex,

Lin *et al. Journal of Neuroinflammation*   (2024) 21:220

Page 8 of 23

and cerebellum regions (Fig. 1C, D, E, F). Figure 1C illustrates representative PeriCam laser speckle images of rCBF before, 10 min, 3 days, 7 days, 14 days, and 28 days after either Sham or BCAS surgery. As shown in Fig. 1C, D, there were no significant changes in rCBF in in the cerebral hemispheres of the Sham Ctrl group between the pre-surgery baseline and 3–28 days post-surgery time points (p > 0.05, Fig. 1C, D). In contrast, the BCAS group exhibited an approximately 20% decrease in hemispheric rCBF at 10 min post-BCAS surgery (**p < 0.01) and this cerebral hypoperfusion sustained at 3–28 days post-BCAS (*p < 0.05, **p < 0.01, respectively, Fig. 1C, D). In addition, we have analyzed CBF changes in the cerebral frontal cortex and cerebellum in the Sham and BCAS brains (Fig. 1E, F and Supplemental Figure S1C, D). It shows that BCAS male mice displayed reduced rCBF in the frontal cortex regions approximately by 25% (10 min post-BCAS) and by 18% (3 days post-BCAS) (****p < 0.0001, *p < 0.05, Fig. 1E). Additionally, the rCBF in the cerebellum also decreased significantly at 10 min (by ~ 29%) and at 3 days (by 21%) post-BCAS (****p < 0.0001, *p < 0.05, Fig. 1F). By 7 days post-BCAS, the rCBF in both regions had recovered to > 90% of the baseline levels (p > 0.05, Fig. 1E, F).

Since vascular dementia appears to be more common in males in clinical settings, we assessed whether male and female mice displayed different responses after BCAS. In female mice, the rCBF in the cerebral frontal and cerebellum regions decreased by approximately 24% and 20%, respectively, at 10 min post-BCAS surgery (*p < 0.05, **p < 0.01, Figure S1C, D). By 3 days post-surgery, the rCBF in both regions had recovered to > 90% of the baseline levels (p > 0.05, Figure S1C, D). The female mice dropped approximately 4–5% more in the CBF of hemispheres than in males at 10 min post-BCAS (Supplemental Figure S1E, p > 0.05) but followed with a faster recovery (a 9%-10% CBF increase) during the compensation period from 3 to 28 days post-BCAS (Figure S1 E, p > 0.05). This sex difference is consistent with human studies, as vascular dementia, which is caused by a reduction of blood flow to the brain, is more frequent in males [27], perhaps pointing to reduced compensation of blood flow after neurovascular events in males. Due to early recovery of the rCBF in female mice post-BCAS, we only conducted experiments in male mice in the rest of the study.

BCAS induces changes of ChP SPAK-NKCC1 protein complex

We then investigated whether BCAS-induced any changes of ChP structures. Figure 2A illustrate three regions of interest (ROI 1–3) selected from each side of the LVCP. We examined whether BCAS triggers changes of the ChP secretory ion transport protein complex SPAK-NKCC1. Sham ChP show total non-phosphorylated SPAK and NKCC1 protein enriched at the apical (luminal) membrane of ChP epithelial cells, but less in the basolateral membrane. In contrast, BCAS mice displayed sustained upregulation of both total NKCC1 protein (~ 1.85-, ~ 2.55- or 2.83-fold, respectively) and pNKCC1 protein (~ 1.88-, ~ 1.85-, ~ 2.65-) at 4-, 6- and 8-weeks post-BCAS (*p < 0.05, **p < 0.01, Fig. 2B, C, D, E.). However, the regulatory serine-threonine kinases SPAK and phosphorylated SPAK (pSPAK) showed opposite responses, with initial significant reduction of apical SPAK expression (by 46%) (**p < 0.01, Fig. 2B, C), but elevated pSPAK protein expression by twofold at 4-weeks post-BCAS (*p < 0.05, Fig. 2D, E). At 6-weeks post-BCAS, SPAK levels significantly increased to twice that of the Sham Ctrl, and by 8-weeks post-BCAS, SPAK immunostaining intensity nearly returned to the basal levels (**p < 0.01, *** < 0.001, Fig. 2B, C). pSPAK began to return to the basal levels starting at 6-weeks post-BCAS (*p < 0.05, Fig. 2D, E). Taken together, these data demonstrate that BCAS causes dynamic changes of ChP secretion function-related proteins SPAK and NKCC1 at 4–8 weeks post-BCAS.

BCAS mice display neurological behavioral deficit and sensitivity to SPAK inhibitor ZT-1a treatment at 2–4 weeks post-BCAS

We next assessed whether BCAS triggered neurological deficits in mice, and if they were sensitive to SPAK inhibitor ZT-1a treatment. C57BL/6 J male mice were subjected to sham or BCAS surgery with treatment regimens with either BCAS + Veh (100% DMSO, 2 ml/kg body weight/day) or BCAS + ZT-1a (5 mg/kg body weigh/day, i.p.) at 14–28 days post-surgery (Fig. 3A). The neurological function was determined with Open Field (OF) and Y maze tests. In the OF tests, the total distance traveled is used to assess the exploratory behavior and activity inclination of mice, while the number of vertical activity counts is used to evaluate exploratory behavior and curiosity [29, 30]. Compared to the sham group, the BCAS + Veh group showed a marked reduction in both total travel distance (by 58%, **p < 0.01) and vertical activities (by 54%, *p < 0.05, Fig. 3B, C), revealing reduced locomotor activity and exploratory drive at 4-weeks post-BCAS. However, the BCAS + ZT-1a group displayed similar performance on total travel distance and vertical activity counts as the sham group (Fig. 3B, C). These findings suggest that BCAS-induced anxiety and/or motor dysfunction can be effectively mitigated by pharmacological blockade of SPAK protein using the SPAK inhibitor ZT-1a at 2–4 weeks post-BCAS. In testing changes of spatial working memory in these mice in the Y-maze
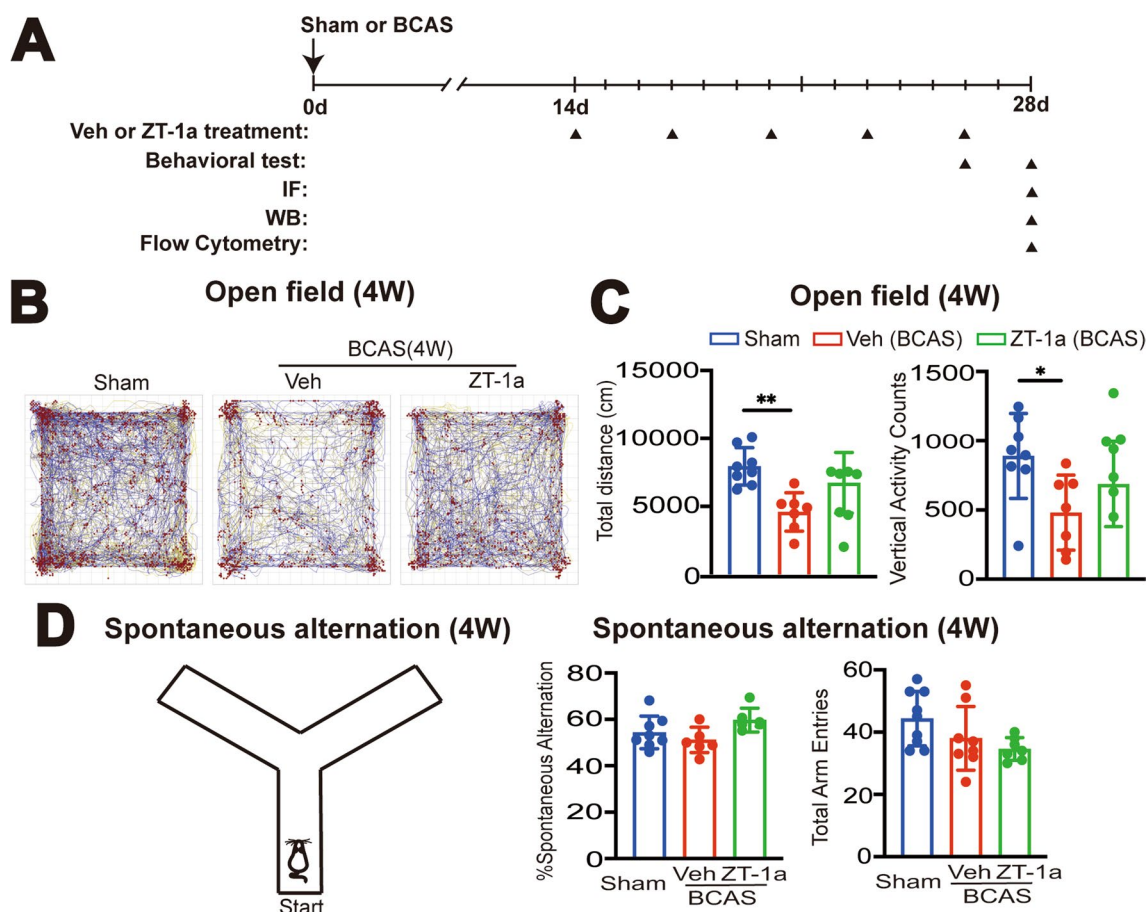
Lin *et al. Journal of Neuroinflammation*   (2024) 21:220

Page 9 of 23

Fig. 3 Administration of SPAK inhibitor ZT-1a at 2–4 weeks post-BCAS attenuates neurological behavioral deficits in mice. **A** Experimental protocol. C57BL/6 J mice underwent sham or BCAS surgery. BCAS mice received either vehicle (100% DMSO, 2 ml/kg body weight/ day) or ZT-1a (5 mg/kg body weigh/day) via intraperitoneal injection (i.p.) from 14 to 28 days. Arrowheads: indicate the time points at which drug treatment, behavior, IF, WB or flow cytometry were performed. **B** Illustration of animal total distance traveled in the Open field test. **C** Summary of travel distance and vertical movement counts. Data are represented as mean ± SD. n = 7–8 mice. *p < 0.05, **p < 0.01. One-way analysis of variance (ANOVA). **D** Y-maze spontaneous alternation test. The percentage of spontaneous alternation and total entry in Y maze test was shown. Data are mean ± SD, n = 6–8 mice. *p < 0.05. One-way analysis of variance (ANOVA)

test, there were no differences in the total arm entries or spatial working memory among the three groups of mice (p > 0.05, Fig. 3D).

Considering that cerebral hypoperfusion has been reported to induce optic nerve damage and visual impairment [31], which could affect the outcomes of neurological behavioral tests, we assessed reactive astrocyte activation in optic nerves of the Sham and BCAS-Veh, and BCAS-ZT-1a brains. As shown in Supplemental Figure S3, the optic nerve of Sham mice exhibited low astrocytic GFAP mean fluorescence intensity (MFI). Some localized elevation in astrocytic GFAP MFI was detected in the optic nerves of some BCAS-Veh mice, however, overall differences between the Sham and BCAS-Veh mice are not statistically significant (p > 0.05, Figure S3A, B). These data suggest that the BCAS model in mice did not cause severe optic nerve damage at 4 weeks post-BCAS, which

is consistent with previous report on a mild demyelination in the optic tract post-BCAS [32]. The lack of the optical nerve damage in the BCAS mouse model could be due to preserved blood flow in the ophthalmic branch artery [33, 34]. Interestingly, the optic nerves of BCAS-ZT-1a mice displayed significantly attenuated GFAP MPI, compared to the Sham or BCAS-Veh group while without performance differences among the three groups in the Y-maze test. These data further imply that potential contribution of the differences in optic nerve damage or visual capacity is negligible in assessing the OFT and Y-maze tests at 4-weeks post-BCAS.

Lin *et al. Journal of Neuroinflammation*   (2024) 21:220

Page 10 of 23

SPAK inhibitor ZT-1a reduces stimulation of ChP pSPAK-pNKCC1 complex and pNF-kB protein at 2–4 weeks post-BCAS

We then evaluated the effect of pharmacological inhibition of SPAK protein on SPAK-NKCC1 complex activation and NF-κB activation. In the Veh-treated BCAS brain, the expression levels of pSPAK and pNKCC1 (arrows) in the ChP were elevated by twofold and threefold, respectively, compared to the Sham Ctrl (*p < 0.05 for pSPAK, ***p < 0.001 for pNKCC1, Fig. 4A, B). In contrast, treatment with ZT-1a prevented such upregulation of pSPAK and pNKCC1 in the ChP epithelial cells of the BCAS + ZT-1a brains, which showed at 80% and 70% of the Sham Ctrl levels (Fig. 4A, B). This is significantly different from data in the BCAS + Veh ChP (**p < 0.01 for pSPAK, ****p < 0.0001 for pNKCC1). SPAK functioning as an inflammatory node involves NF-κB activation [12, 13]. We further evaluated changes of pNF-κB protein in ChPs from the BCAS + Veh and the BCAS + ZT-1a brains. NF-κB dimers (p65/p50) are normally sequestered in the cytoplasm by inhibitory factor-KB proteins (IκBα/β/ε). However, when the IκB kinase (IκK) becomes activated, it phosphorylates IκB, causing its dissociation. This enables the NF-κB complex to translocate from the cytosol to the nucleus, initiating transcription [18]. Sham Ctrl showed low expression levels of NF-κB or pNF-κB in the choroid plexus epithelial cells (Fig. 4C, D). But, in the Veh-treated BCAS brain, pNF-κB (Ser536) in the choroid plexus epithelial cells was increased significantly (2.29-fold), compared to the Sham Ctrl (****p < 0.0001, Fig. 4D), while the rise in NF-κB expression was less pronounced (p > 0.05). Administration of the SPAK inhibitor ZT-1a post-BCAS reduced the upregulation of pNF-κB by 56% (****p < 0.0001, Fig. 4D). To further detect changes of nuclear p-NF-kB signals, using Imaris reconstruct tool (the spot tool), we quantified changes of p-NF-κB immunostaining signals within the DAPI$^+$-reconstructed structures (Fig. 4D). For each stack image, the "total number of p-NF-κB immunostaining spots" were divided by the "total number of DAPI$^+$ surfaces" to represent p-NF-κB puncta density in the nucleus. Figure 4D showed that the BCAS + Veh ChP epithelial cells showed a 1.39-fold increase in the p-NF-κB puncta density compared to the Sham Ctrl (*p < 0.05, Fig. 4D). But the BCAS + ZT-1a ChP illustrated a 35% reduction of the p-NF-κB puncta density compared with the BCAS + Veh ChP (p = 0.1681, Fig. 4D). These data demonstrate the involvement of SPAK in the post-BCAS induced activation of pNF-κB inflammatory pathway.

Changes of the SPAK-NKCC1 complex in LVCP at 4 weeks post-BCAS were also analyzed in immunoblots. LVCP homogenates from the Sham, BCAS + Veh and BCAS + ZT-1a brains showed similar levels of expression of SPAK and pSPAK proteins, NKCC1 and pNKCC1 proteins or claudin-1 (p > 0.05, Supplemental Figure S4A, B, C, D). With LVCP tissue homogenates (no isolation of cytosolic and nuclear fractions due to small cell numbers), no differences in NF-kB expression were detected among Sham, the BCAS + Veh and the BCAS + ZT-1a ChPs (p > 0.05, Figure S4E, F). The discrepancies between findings of immunofluorescence staining and immunoblotting approaches could be that Western blotting probes protein levels (SPAK, NKCC1, NF-kB, pNF-κB) across the entire LVCP, while immunofluorescence analysis enables to detect localized changes within specific ChP ROI regions of epithelial cells. The discrepancy between the immunostaining and immunoblot data could also result from heterogenous CBF hypoperfusion within the LVCP, the heterogenous damage of ChP can be detected by the immunostaining analysis of specific ROI but got lost in the whole LVCP homogenate preparation.

Pharmacological inhibition of the SPAK–NKCC1 complex at 2–4 weeks post-BCAS reduces brain immune cell infiltration

We further investigated whether BCAS leads to neuroinflammation at 14-28d post-surgery and whether pharmacological inhibition of SPAK attenuates such events. Changes of immune cell infiltration in the cerebral hemisphere or the ChP in the BCAS + Veh or BCAS + ZT-1a mice were quantified at day 28 post-surgery via flow cytometry analysis. Compared to the Sham Ctrl, the BCAS + Veh cerebral hemisphere exhibited a significant increase in the number of CD11b$^+$CD45^{+hi} myeloid cells (by twofold, *p < 0.05, Fig. 5A). In contrast, 50% reduction was detected in the number of CD11b$^+$CD45^{+lo} myeloid cells (**p < 0.01, Fig. 5A). Additionally, a 1.63-fold increase in CD11b$^+$CD45$^+$/Ly6G$^+$ neutrophils (*p < 0.05,

(See figure on next page.)

Fig. 4 ZT-1a treatment at 2–4 weeks post-BCAS attenuates SPAK-NKCC1 complex and pNF-kB activation. **A** Representative immunofluorescent staining image of pSPAK and pNKCC1 in the Sham or BCAS + Veh, BCAS + ZT-1a LVCPs. Arrowheads: low level expression of pSPAK or pNKCC1. Arrows: elevated pSPAK or pNKCC1 expression. **B** Quantification summary. Data are mean ± SD (n = 4 mice). *p < 0.05, **p < 0.01, ***p < 0.001, ****p < 0.0001. One-way analysis of variance (ANOVA). **C**. Representative immunofluorescent staining Max IP image of NF-κB and pNF-κB, and 3D cell reconstruction images of nuclear pNF-kB. **D** Quantification summary. Data are mean ± SD (n = 4–6 mice). *p < 0.05, ****p < 0.0001 vs Sham. One-way analysis of variance (ANOVA), One Sample t-test or unpaired t-test
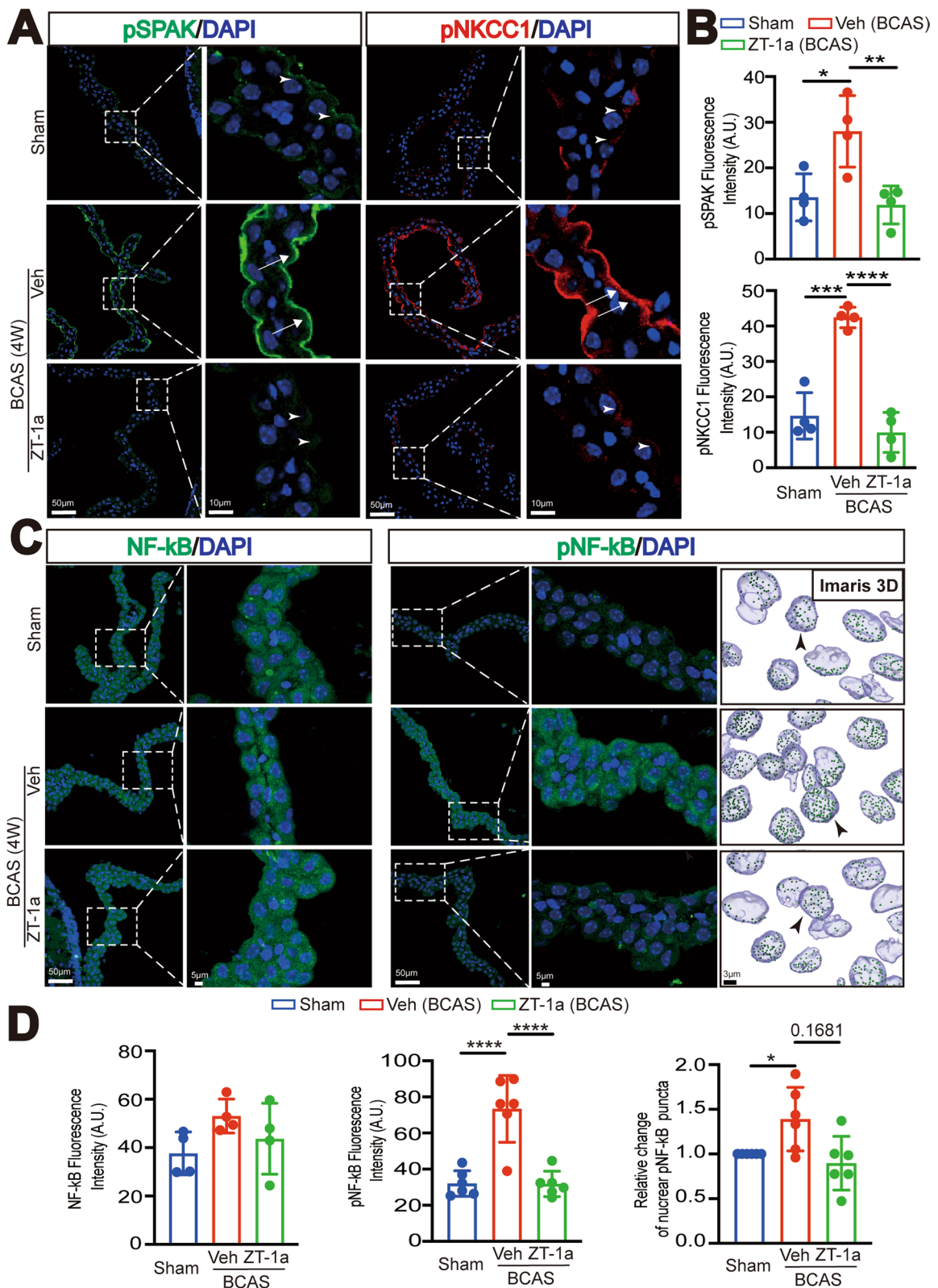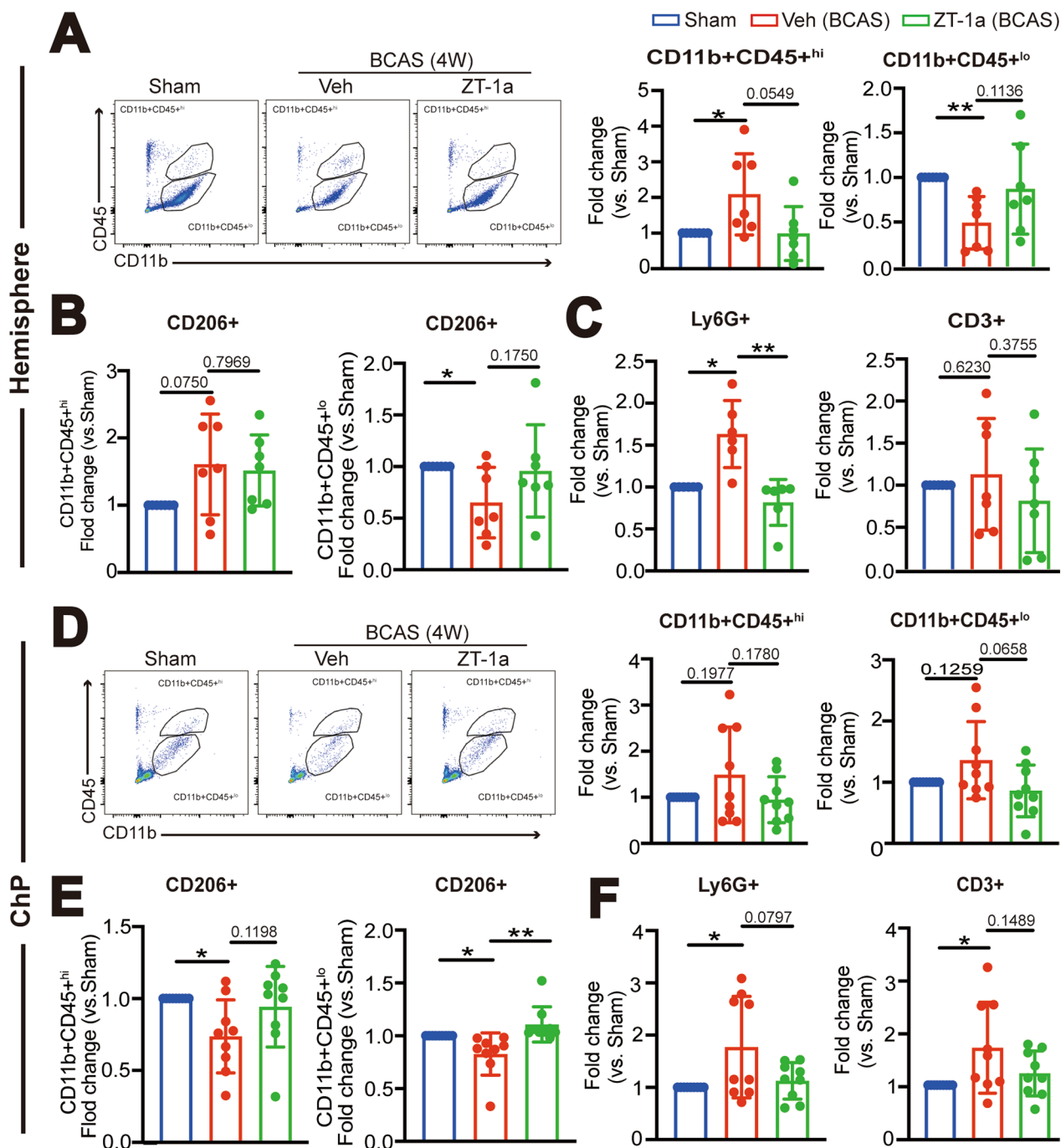
Fig. 4 (See legend on previous page.)

Fig. 5 Administration of ZT-1a at 2–4 weeks post-BCAS reduces immune cell infiltration into hemisphere and ChP. **A** Representative flow cytometric plots of CD11b$^+$CD45^{+hi} or CD11b$^+$CD45^{+lo} myeloid cells from cerebral hemisphere at 4 weeks post-BCAS surgery with the percentage of total number of CD11b$^+$CD45^{+hi} or CD11b$^+$CD45^{+lo} myeloid cells in the single cells. Data are mean ± SD (n = 7 mice). *P < 0.05, **p < 0.01. One Sample t-test. Unpaired t-test. **B** Percentage of anti-inflammation CD11b$^+$CD45^{+hi}/CD206$^+$ and CD11b$^+$CD45^{+lo}/CD206$^+$ cells. Data are mean ± SD (n = 7 mice). *p < 0.05. One Sample t-test. Unpaired t-test. **C**. The percentage of total number of CD3$^+$ lymphocyte in the single cells and CD11b$^+$CD45$^+$/ Ly6G$^+$ neutrophils. Data are mean ± SD (n = 8 mice). *p < 0.05, **p < 0.01. One Sample t-test. Unpaired t-test. **D** Representative flow cytometric plots of CD11b$^+$CD45^{+hi} or CD11b$^+$CD45^{+lo} myeloid cells from the LVCP and the percentage in the single cells. Data are mean ± SD (n = 8–9 mice). One Sample t-test. Unpaired t-test. **E** Percentage of anti-inflammatory CD11b$^+$CD45^{+hi}/CD206$^+$ and CD11b$^+$CD45^{+lo}/CD206$^+$ cells. Data are mean ± SD (n = 8–9 mice), *p < 0.05, ** < 0.01. One Sample t-test. Unpaired t-test. **F** The percentage of total number of CD3$^+$ lymphocyte and CD11b$^+$CD45$^+$/ Ly6G$^+$ neutrophils in the single cells. Data are mean ± SD (n = 8–9 mice), *p < 0.05. One Sample t-test. Unpaired t-test

Lin *et al. Journal of Neuroinflammation*   (2024) 21:220

Page 13 of 23

Fig. 5C) and a 35% decrease in CD11b$^+$CD45^{+lo}/CD206$^+$ anti-inflammatory myeloid cells was detected in the BCAS + Veh cerebral tissues (*p < 0.05, Fig. 5B). No significant changes in CD3$^+$ T cells were observed (p = 0.6230, Fig. 5C), compared to the sham Ctrl. In contrast, the BCAS + ZT-1a cerebral hemisphere tissues displayed reduced quantity of CD11b$^+$CD45^{+hi} cells (p = 0.0549, Fig. 5A), increased anti-inflammatory CD11b$^+$CD45^{+lo}/CD206$^+$ myeloid cells (p = 0.1750, Fig. 5B), and reduced infiltration of neutrophils (**p < 0.01, Fig. 5C).

In flow cytometry analysis of immune cell infiltration in the ChPs, the landscape is very different. Compared to the sham Ctrl, the BCAS + Veh ChPs exhibited less increase in CD11b$^+$CD45^{+hi} and CD11b$^+$CD45^{+lo} myeloid cells (p = 0.1977, p = 0.1259, Fig. 5D). However, a significant reduction of CD11b+CD45^{+hi}/CD206$^+$ (26%) and CD11b$^+$CD45^{+lo}/CD206$^+$ (18%) myeloid cells were detected (*p < 0.05, Fig. 5E). An obvious increase in CD11b$^+$CD45$^+$/Ly6G$^+$ neutrophils (*p < 0.05, Fig. 5F) and a 1.68-fold increase in CD3$^+$ T cells (*p < 0.05, Fig. 5F) were detected in the BCAS + Veh ChPs at 4-weeks post-BCAS. Treatment with ZT-1a normalized the level of anti-inflammatory CD11b$^+$CD45^{+hi}/CD206$^+$ and CD11b$^+$CD45^{+lo}/CD206$^+$ myeloid cells near to the sham Ctrl levels (p = 0.1198, **p < 0.01, Fig. 5E), while also reducing the infiltration of neutrophils and CD3$^+$ T cells into the ChP (p = 0.0797, p = 0.1489, Fig. 5F).

To further assess changes immune cell infiltration in the cortex, peri-ventricle, and ChP regions, we performed immunofluorescence staining for Iba1$^+$ cells in these regions. Compared to the Sham group, the number of Iba1$^+$ cells was significantly increased in the peri-ventricle region of the BCAS + Veh brains (*p < 0.05, Supplemental Figure S5A, C), a less profound elevation was detected in the cortex and ChP (p > 0.05, Figure S5A, C). Consistently, the BCAS + ZT-1a brains (the cortex, peri-ventricle, or ChP regions) did not show statistically significant changes in Iba1$^+$ counts, compared to the Sham Ctrl (p > 0.05, Figure S5A, C). In summary, these findings clearly demonstrate a role of the SPAK in immune cell infiltration in BCAS cerebral tissues and ChP.

ZT-1a administered at 4–8 weeks post-BCAS remains protective

We further investigated whether administration of SPAK inhibitor ZT-1a during 4–8 weeks post-BCAS remains protective against hypoperfusion-induced damage. The BCAS + Veh mice (100% DMSO, 2 ml/kg body weight/day) or BCAS + ZT-1a mice (5 mg/kg body weight/day, i.p.) received treatment regimens from day 28 to 56 post-BCAS, as shown in Fig. 6A. The sham Ctrl group did not show significant changes in rCBF between the pre-surgery baseline throughout 8-weeks post-surgery

(p > 0.05). In contrast, the BCAS + Veh mice exhibited an approximate 40% reduction in rCBF at 8-weeks post-BCAS (***p < 0.001, Fig. 6B, C). Interestingly, in the BCAS + ZT-1a mice, the rCBF was preserved at 83% of the pre-surgery level, showing significantly less hypoperfusion (*p < 0.05, Fig. 6B, C). In assessing their performance in the Y-maze for the Spontaneous Alternation and Novel Spatial Recognition (NSR) tests, the BCAS + Veh mice showed 20% reduction in the spontaneous alternation test, indicating deficits in spatial working memory (*p < 0.05, Fig. 6D), which was absent in the BCAS + ZT-1a group (**p < 0.01, Fig. 6D). These findings were further supported by the Recognition Index data of the NSR test, which was defined as the duration in novel arm divided by the total duration spent on both familiar and novel arms, to represent changes in the mice's curiosity towards previously unvisited areas. The Sham Ctrl group exhibited an intact working memory with a higher recognition index. In contrast, the BCAS + Veh group showed 34% reduction in the Recognition Index (**p < 0.01, Fig. 6E). The BCAS + ZT-1a mice did not display any differences from the Sham Ctrl group (Fig. 6E). Taken together, these findings clearly show that pharmacological blockade of SPAK protein with ZT-1a at 4–8 weeks post-BCAS can effectively improve the recovery of CBF as well as preserving spatial working memory.

ZT-1a-mediated sustained attenuation of immune cell infiltration into the cortical hemisphere and ChP treatment

We then assessed whether post-BCAS ZT-1a administration reduced immune cell infiltration in the cerebral hemisphere and ChP at 8-weeks post-BCAS. The flow cytometry analysis revealed that at 8-weeks post-BCAS, there was a persistent increase in the number of CD11b$^+$CD45^{+hi} myeloid cells, but not the CD11b$^+$CD45^{+lo} myeloid cells, in the cerebral cortical hemisphere of the BCAS + Veh mice, compared to the sham Ctrl (**p < 0.01, Fig. 7A). Additionally, CD3$^+$ T cells in the BCAS + Veh cerebral hemisphere remained significantly elevated (*p < 0.05, Fig. 7C), accompanied with a 25% decrease in CD11b+CD45^{+hi}/CD206$^+$ myeloid cells (*p < 0.05, Fig. 7B). In contrast, the immune cell infiltration profiles in the BCAS + ZT-1a cerebral hemisphere are significantly different, with a reduction of CD11b$^+$CD45^{+hi} (p < 0.05, Fig. 7A) and CD3$^+$T cell infiltration (**p < 0.01, Fig. 7C) and an increase in anti-inflammatory CD11b$^+$CD45^{+hi}/CD206$^+$ myeloid cells (p = 0.2835, Fig. 7B). Interestingly, in the ChP, the BCAS + Veh mice showed sustained 2.3-fold increase in CD11b$^+$CD45$^+$/Ly6G$^+$ neutrophils, while no significant changes in anti-inflammatory myeloid cell or CD3$^+$ T cell infiltration, indicating partial recovery from inflammatory responses by 8-weeks post-BCAS. In contrast,

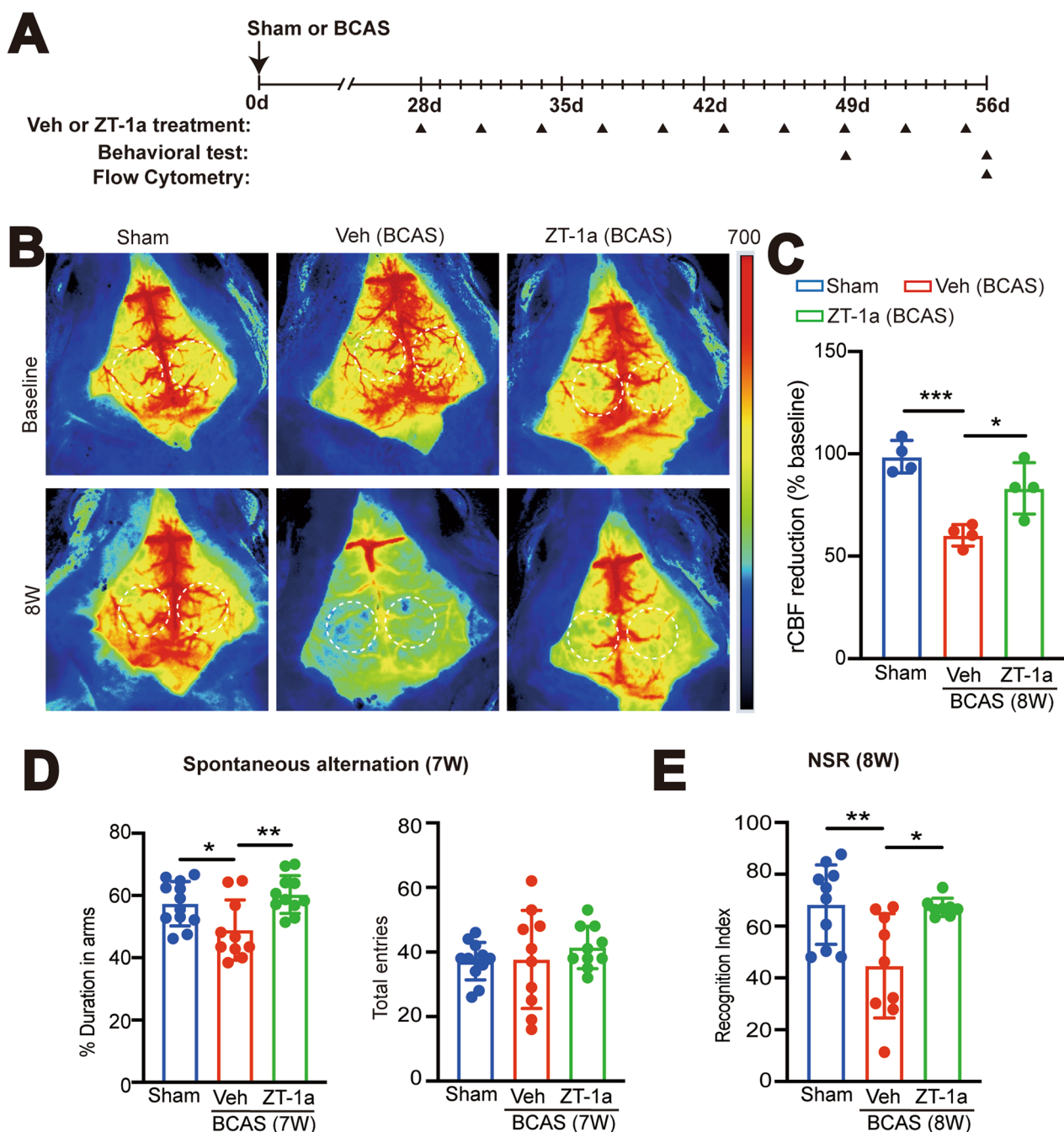Lin *et al. Journal of Neuroinflammation*   (2024) 21:220

Page 14 of 23

Fig. 6 Protective effects of SPAK inhibitor ZT-1a at 4–8 weeks post-BCAS. **A** Experimental protocol. C57BL/6 J mice underwent sham, BCAS + Veh (100% DMSO, 2 ml/kg body weight/ day, i.p.), or BCAS + ZT-1a (5 mg/kg/day, via intraperitoneal injection, i.p.) at 28-56d. Arrowheads: indicate the time points at which drug treatment, CBF or behavioral test were performed **B** Representative periCam PSI images of rCBF at 56 days (8-weeks) after surgery. Dashed circle: region of interest (ROI). **C** Quantification analysis of rCBF. Data are expressed as mean ± SD. n = 4 mice. *p < 0.05, ***p < 0.001 vs. Sham. One-way analysis of variance (ANOVA). **D** The percentage of spontaneous alternation and total entry in Y maze test. n = 10–12 mice. *p < 0.05, **p < 0.01. One-way analysis of variance (ANOVA). **E** The recognition index of the Novel Spatial Recognition (NSR) test. Data are represented as mean ± SD. n = 8–10 mice. *p < 0.05, ** < 0.01 vs. sham. One-way analysis of variance (ANOVA)

the $CD11b^+CD45^+/Ly6G^+$ neutrophil infiltration into the ChP was absent in the BCAS + ZT-1a brains (**p < 0.01, Fig. 7F). These findings indicated the evolution of neuroinflammation between 4 and 8 weeks post-BCAS.

Blocking the SPAK-NKCC1 complex with ZT-1a attenuated BCAS-induced immune cell infiltration into the cerebral hemisphere and ChP.
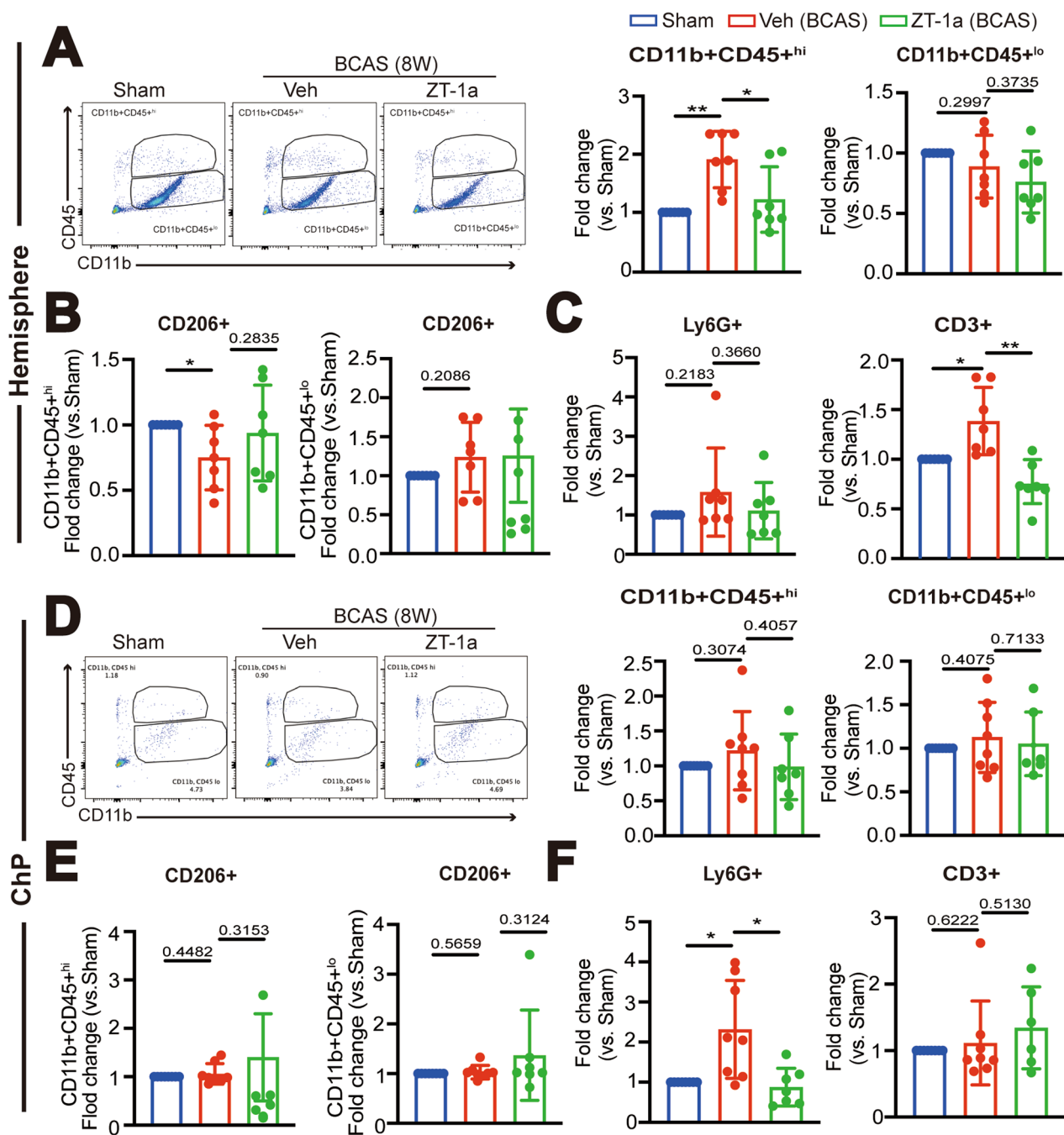
Fig. 7 ZT-1a treatment at 4–8 weeks post-BCAS attenuated chronic immune cell infiltration into the hemisphere and ChP. **A** Representative flow cytometric plots of CD11b+CD45+ hi or CD11b+CD45+lo myeloid cells in the single cells from hemisphere at 8-weeks post-surgery. Data are mean ± SD (n = 7 mice). *P < 0.05, **p < 0.01. One Sample t-test. Unpaired t-test. **B** Fold changes of anti-inflammation CD11b+CD45+hi/ CD206+ and CD11b+CD45+lo/CD206+ cells. Data are mean ± SD (n = 7 mice). *p < 0.05. One Sample t-test. Unpaired t-test. **C** Fold changes of total number of CD3+ lymphocyte and CD11b+CD45+/Ly6G+ neutrophils. Data are mean ± SD (n = 7 mice). *p < 0.05, ** p < 0.01. One Sample t-test. Unpaired t-test. **D** Representative flow cytometric plots of CD11b+CD45+hi or CD11b+CD45+lo myeloid cells from the LVCP and the percentage in the single cells. Data are mean ± SD (n = 7–8 mice). One Sample t-test. Unpaired t-test. **E** Fold changes of anti-inflammatory CD11b+CD45+hi/ CD206+ and CD11b+CD45+lo/CD206+ cells. Data are mean ± SD (n = 7–8 mice), p > 0.05. One Sample t-test. Unpaired t-test. **F** Fold changes of CD3+ lymphocyte and CD11b+CD45+/Ly6G+ neutrophils in the single cells. Data are mean ± SD (n = 7–8 mice), *p < 0.05. One Sample t-test. Unpaired t-test

Lin *et al. Journal of Neuroinflammation*   (2024) 21:220

Page 16 of 23

Pharmacological inhibition of the SPAK–NKCC1 complex preserves the ChP blood-CSF barrier structure in BCAS brains

To further investigate whether pharmacological inhibition of SPAK protein protects the blood-CSF barrier, we examined changes of claudin-1 expression in the ChP epithelial cells in the Veh vs ZT-1a treated mice at 4-weeks post-BCAS. In the Sham ChP, the normal location of claudin-1 TJ proteins was observed between the epithelial cells of the ChP (Fig. 8A). In the BCAS + Veh ChP, there was a significant increase in the immunofluorescence intensity of claudin-1, approximately 1.8 times higher than that of the Sham group (*$p < 0.05$, Fig. 8A, B), that especially appeared near the epithelial apical membranes (as indicated by sector-shaped box and arrow, *$p < 0.05$, Fig. 8A, B). IMARIS 3D reconstruction of these images illustrated that BCAS-induced loss of polarity of claudin-1 protein expression at the ChP epithelial cells (as indicated by arrowhead), with the increased volume of claudin-1$^+$ stained structure than the Sham Ctrl (*$p < 0.05$, Fig. 8A, C), collectively indicating maldistribution of TJ proteins at the blood-CSF barrier after BCAS. In contrast, in the BCAS + ZT-1a ChPs, the immunofluorescence intensity of claudin-1 and its abnormal location at the apical membranes of ChP epithelial cells were decreased to a level like the Sham Ctrl (*$p < 0.05$, Fig. 8A, B). We further investigated changes in expression of claudin-5 and E-cadherin in the ChP at 4-weeks post-BCAS. In Sham ChP, the claudin-5 protein was primarily expressed in ChP epithelial cells (Fig. 9A). The immunofluorescence intensity of claudin-5 was significantly increased in the BCAS + Veh ChP, compared to the Sham group (by 2.7-fold, *$p < 0.05$, Fig. 9A, C). In contrast, such a change in claudin-5 in the BCAS + ZT-1a Chp is not significant ($p = 0.0865$, Fig. 9A, C). As for E-cadherin, it was abundantly distributed in the ChP epithelial cells (Fig. 9B), which was elevated in the BCAS + Veh group ($p = 0.1407$, Fig. 9B, D). Taken together, BCAS triggered changes of claudin-1, claudin-5, and E-cadherin proteins in a similar trend. To further assess if the permeability of the blood-CSF barrier is compromised at 4-weeks post BCAS, we conducted an initial evaluation by measuring albumin leakage into the CSF. We measured albumin levels in the CSF and serum from the Sham, BCAS + Veh,

and BCAS + ZT-1a mice at 4 weeks post-BCAS. The ratio of CSF Albumin/Serum Albumin in the BCAS + Veh mice was 1.34-fold of the Sham mice ($p = 0.4940$, Fig. 9E). The BCAS + ZT-1a mice displayed a similar value in the CSF Albumin/Serum Albumin ratio ($p = 0.3595$). These data indicate that despite of BCAS-induced cellular structural changes in the blood-CSF barrier, its permeability for large proteins such as albumin (66.5 kDa) is not compromised (Fig. 10).

Discussion

Chronic cerebral hypoperfusion-mediated changes of ChP

Previous research identified reduction of the blood-CSF barrier integrity in AD patients through downregulation of TJ proteins, including claudin-1 and -5, and upregulation of matrix metalloproteases [35]. This leads to overall atrophy of the ChP and subsequent diminished Aβ clearance [36]. There are also changes in immune signaling at the ChP of dementia patients of the AD type with decreased leukocyte trafficking but increased levels of IFN-γ and TNF-α [35, 37]. In our study, using the carotid artery stenosis-induced chronic cerebral hypoperfusion model, we observed a significant dynamic increase in TJs, such as claudin-1 and claudin-5. The initial increased expression of TJ proteins may represent a compensatory response to the chronic cerebral hypoperfusion pathological conditions, aiming to maintain the integrity of the blood-CSF barrier. However, such upregulation of TJ proteins are not always beneficial, as evidenced by the inflammation-dependent increase in the expression of claudin-1 and claudin-2 in inflammatory bowel disease and their role in early tumor transformation [38]. Furthermore, previous studies have shown that in inactive Crohn's disease, TJ proteins such as claudins dislocate from their normal position at the apical TJs to the basolateral side, potentially misplacing TJ proteins and damaging the barrier function, thereby allowing gut antigens to invade [39]. Moreover, a differential role of TJ proteins in maintaining tight junction stability rather than tight junction assembly has been reported in the intestinal epithelial barrier integrity [40]. We speculate that BCAS-induced changes of ChP epithelial cells TJ expression and polarization may have significant impact on the blood-CSF barrier function. However, measuring albumin levels

(See figure on next page.)

Fig. 8 Effects of ZT-1a on changes of ChP TJ protein expression after BCAS. **A** Representative immunofluorescent staining of claudin-1 in the sham, BCAS + Veh, or BCAS + ZT-1a brains (2–4 weeks post-BCAS) treatment in single-layer images, Z-Stacks Max IP, and 3D cell reconstruction of immunofluorescent staining images derived from these Z-stacks. Arrows and sector-shaped boxes: the ectopic localization of claudin-1 at the apical membrane of the ChP epithelial cells; Arrowheads: expression of claudin-1. **B** Quantification summary. Data are mean ± SD ($n = 5$ mice). *$p < 0.05$. One Sample t-test. Unpaired t-test. **C** Quantification summary. Data are mean ± SD ($n = 5$ mice). *$p < 0.05$. One Sample t-test. Unpaired t-test
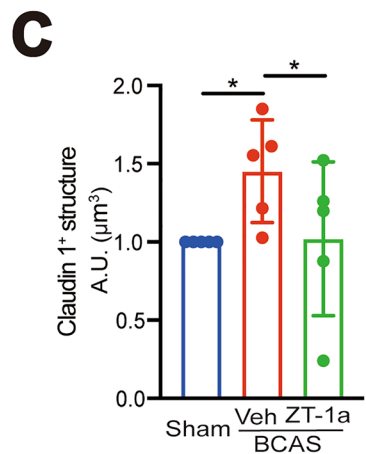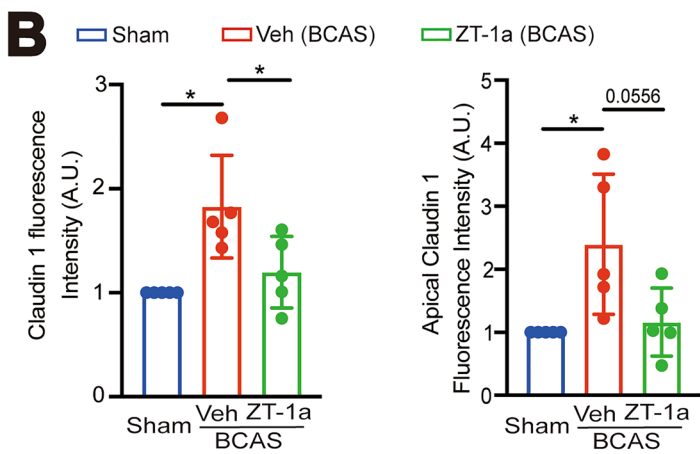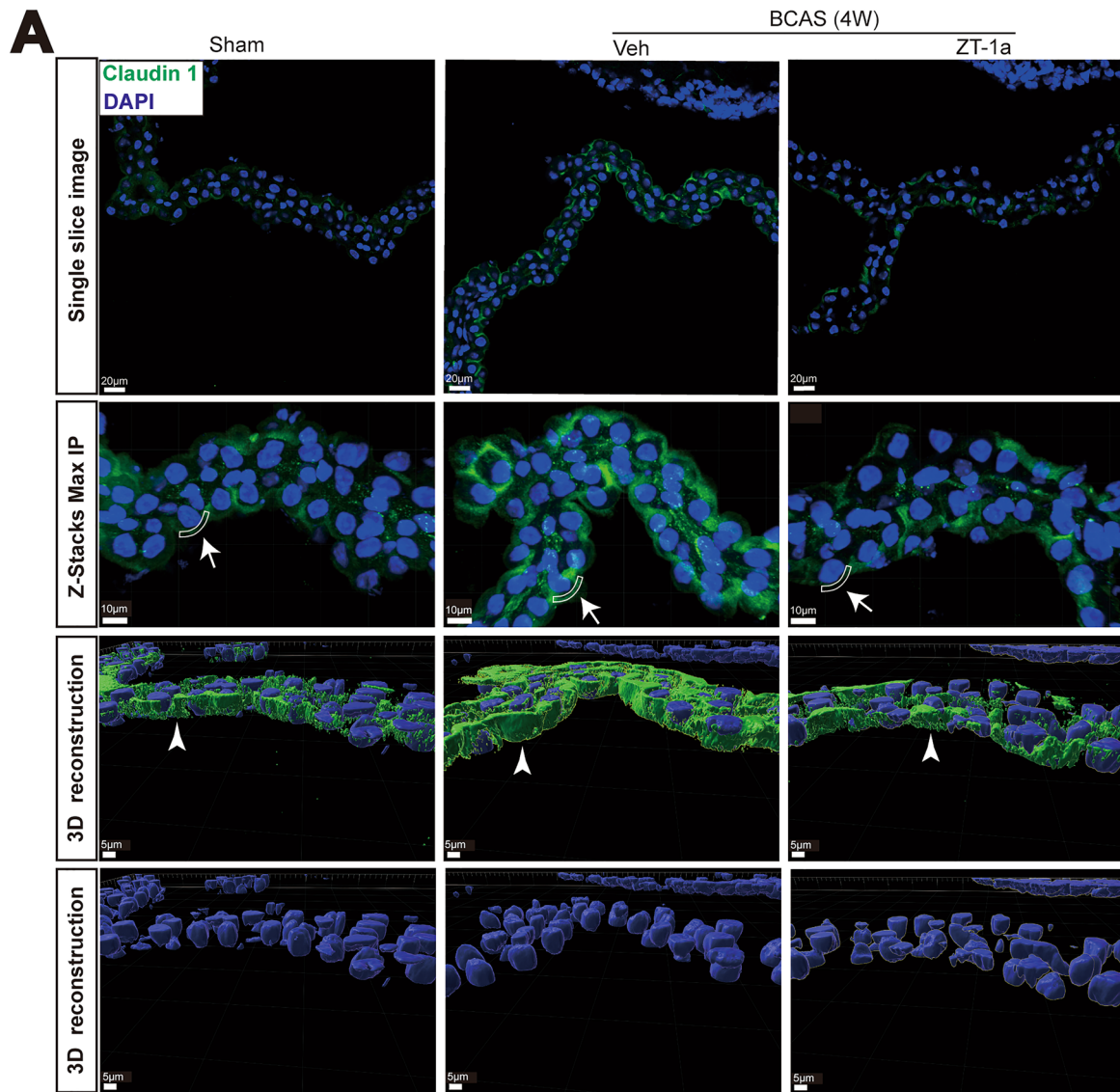
Fig. 8 (See legend on previous page.)

Lin *et al. Journal of Neuroinflammation*   (2024) 21:220
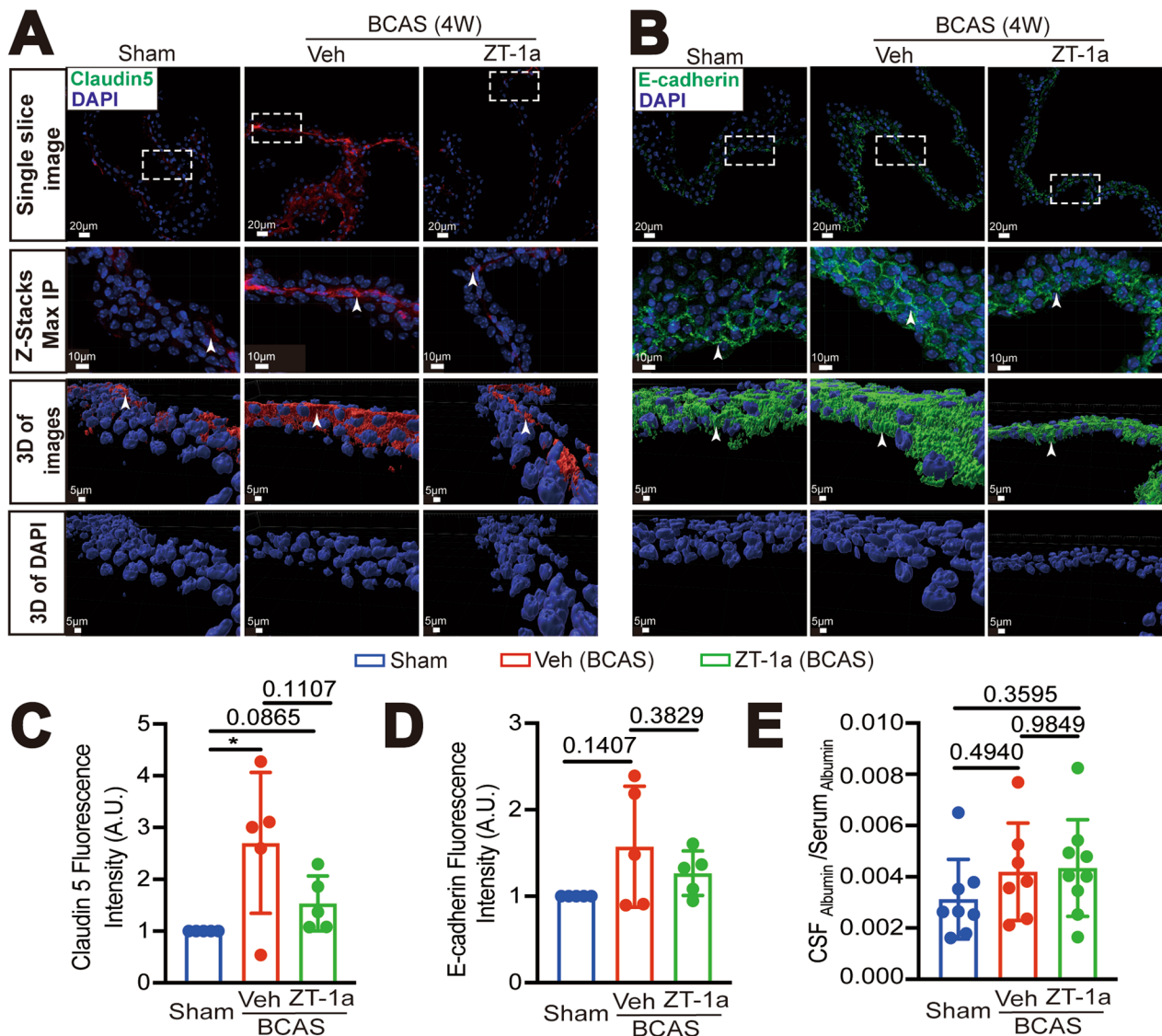
Page 18 of 23

Fig. 9 Effects of ZT-1a on changes of ChP claudin-5 and E-cadherin expression after 4 weeks post-BCAS. **A** Representative immunofluorescent staining images of claudin-5 in the sham, BCAS+Veh, BCAS+ZT-1a ChP (including single-layer images, Z-Stacks Max IP, and 3D cell reconstruction images derived from these Z-stacks). Rectangular boxes: indicate the regions presented in the Z-stacks maximum intensity projection (Max IP) and 3D reconstruction images; Arrowheads: indicate the expression of claudin-5. **B** Representative immunofluorescent staining images of E-cadherin. Rectangular boxes: indicate the regions presented in the Z-stacks maximum intensity projection (Max IP) and 3D reconstruction images. Arrowheads: indicate the expression of E-cadherin. **C–E** Quantification summary. Data are mean as ± SD (n = 5 mice). *p < 0.05. One Sample t-test. Unpaired t-test. Quantification of albumin in CSF and serum in **E** was by ELISA

in the CSF and serum from the Sham, BCAS + Veh, and BCAS + ZT-1a mice at 4 weeks post-BCAS did not detect compromised permeability of the blood-CSF barrier for albumin (66.5 kDa). Additional studies are warranted for testing different sizes of permeability tracers.

ChP damage and neuroinflammation

The presence of various immune cells in the ChP have been detected under embryonic, adult, and aged mice,

including macrophages, neutrophils, dendritic cells, and lymphoid cells (B cells and T cells) [41]. During inflammation, the ChP releases cytokines into the CSF, providing a chemotactic driving force for the entry of immune cells into the CNS [28, 41]. In our studies, we found a significant increase in CD3^{+} T-cells and neutrophils in the ChPs at 4 weeks post-BCAS, indicating the active phase of an inflammatory response induced by chronic cerebral hypoperfusion. Additionally, a decrease in
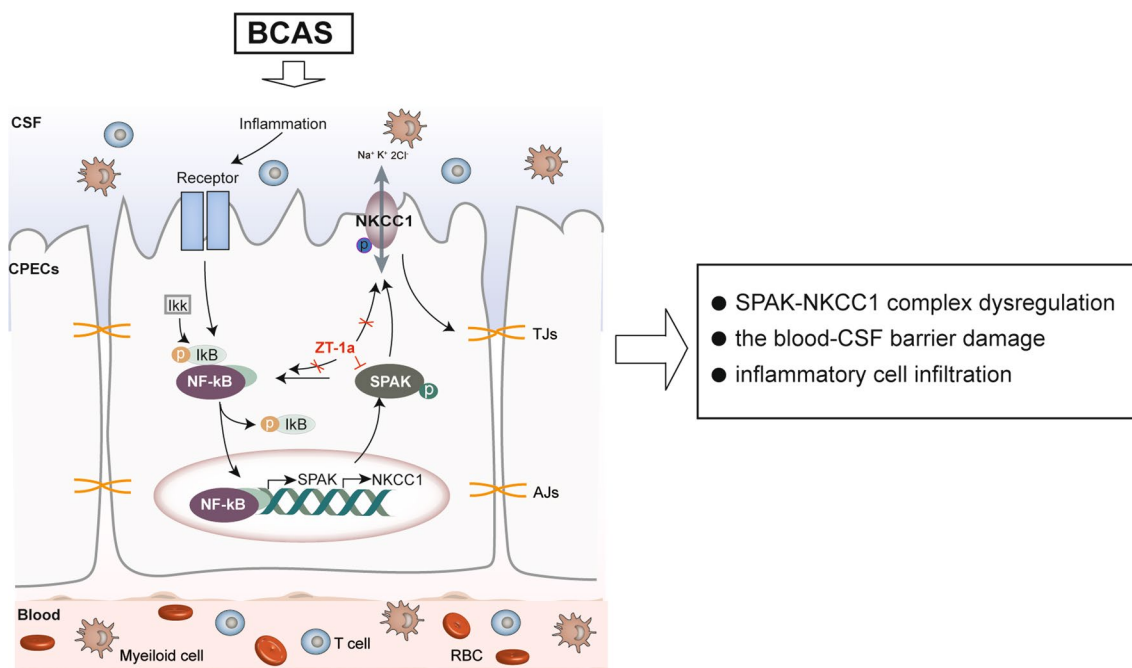
Lin *et al. Journal of Neuroinflammation*   (2024) 21:220

Page 19 of 23

Fig. 10 Schematic summary of the brain-ChP barrier damage after BCAS. The ChP, with tight junctions (TJ) at the apical membrane of the ChP epithelial cells, prevents inflammation by blocking immune cells from entering the brain. Na^+-K^+-Cl^- cotransporter isoform 1 (NKCC1) and its regulatory serine-threonine kinase, SPAK, located at the apical membrane, are essential in regulating choroid plexus epithelial cell volume and CSF secretion/clearance. BCAS stimulates dynamic changes of TJ proteins and the SPAK-NKCC1 complex, which contributes to altered ChP TJ proteins and infiltration of immune cells. Inflammatory signals activate the IκB kinase (IKK) complex, leading to the phosphorylation and dissociation of IκB proteins (IκBα/β/ε) that normally sequester NF-κB dimers (p65/p50) in the cytoplasm. This process allows NF-κB to move from the cytosol to the nucleus, where it promotes the transcription of target genes like SPAK and NKCC1. Pharmacological inhibition of SPAK with its potent inhibitor ZT-1a provides protective effects via attenuating BCAS-induced structural changes at the ChP and neuroinflammation

the anti-inflammatory $CD11b^+CD45^{+hi}/CD206^+$ and $CD11b^+CD45^{+lo}/CD206^+$ myeloid cells were observed. $CD11b^+CD45^{+hi}$ cells represent activated myeloid cells such as macrophages and microglia [42] in exerting pro-inflammatory functions, helping to clear pathogens, and limiting the spread of infection [43]. The number of $CD11b^+CD45^{+lo}$ myeloid cells represents non-activated or resting myeloid cells, including monocytes and microglia under physiological conditions [42]. Our data demonstrate that chronic cerebral hypoperfusion induces phenotypic shift towards a pro-inflammatory state in microglia/macrophages. Moreover, increased percentages of $CD45^+CD11b^+$ cells and $CD45^{+hi}$ $CD11b^+$ $Ly6g^+$ neutrophils have been detected in the ChP of neonatal stroke mice at 3 h post-stroke, with only a few leukocytes entering the ischemic-reperfused cortex [44]. Additionally, at the third day post-transient middle cerebral artery occlusion in adult mice, we previously detected significant increase in pro-inflammatory cells in the ChP, including $CD11b^+CD45^{+hi}$ myeloid cells, $CD11b^+CD45^+Ly6G^-Ly6C^{+hi}$ inflammatory cells, $CD11b^+$ $CD45^+/Ly6G^+$ neutrophils, and $CD3^+$ T cells [15]. Our current study reports novel findings that

the chronic cerebral hypoperfusion triggers sustained inflammatory immune response in the ChP at 4–8 weeks post BCAS. Moreover, a similar inflammatory cell infiltration profile was detected in the cerebral cortex at 4–8 weeks post-BCAS, including increases in neutrophils and $CD11b^+CD45^{+hi}$ myeloid cells and a significant reduction in $CD11b^+CD45^{+lo}$ myeloid cells as well as in anti-inflammatory $CD11b^+CD45^{+lo}/CD206^+$ myeloid populations. This is in contrast to previous report about only increase in $CD68^+$ microglia [45] and a lack of significant changes in the $CD3^+$ and $CD4^+$ lymphocytes in the cortex at 4 weeks post-BCAS [46]. Our new findings expanded information about BCAS-mediated leukocyte infiltration landscape in the cerebral cortex. Taken together, we report here that chronic cerebral hypoperfusion-induced structural damage to the blood-CSF barrier is associated with infiltration of immune cells into both the ChP and cerebral hemispheres.

Impact of pharmacological inhibition of SPAK-NKCC1 complex on the ChP damage

The SPAK-NKCC1 signaling pathway is essential in regulating ChP epithelial cell volume and CSF secretion [47,

48]. The activation of NKCC1 protein plays a pivotal role in the homeostatic regulation of CSF, which can be modulated by the upstream SPAK [12] or directly influenced by the levels of potassium ions within the CSF [14]. Furthermore, the SPAK-NKCC1 complex is instrumental in immune cell signaling during post-hemorrhagic hydrocephalus [12]. The pro-inflammatory cytokine IL-6 significantly increases the abundance of pNKCC1 and pSPAK in cultured choroid plexus epithelial cells [49]. In our study, we discovered that ChP epithelial cells exhibited a continuous increase in total NKCC1 and pNKCC1 proteins from 4 to 8 weeks post-BCAS. In contrast, the regulatory kinase pSPAK only showed a transient elevation at 4 weeks post-BCAS. This motivated us to administer the SPAK protein inhibitor ZT-1a during 2–4 or 4–8 weeks post-BCAS. ZT-1a treatment inhibited the phosphorylatory activation of SPAK and NKCC1 in the ChP at 4 weeks post-BCAS. It also reduced the infiltration of neutrophils and T cells in the ChP and increased the presence of anti-inflammatory CD11bCD45^{hi}/CD206$^+$ and CD11bCD45^{lo}/CD206$^+$ myeloid cells, suggesting that the ChP inflammatory response induced by the chronic cerebral hypoperfusion is attenuated by blocking the SPAK-NKCC1 pathway. It has been noted that SPAK can integrate and conduct environmental stress signals, including NF-κB dependent inflammatory signals [13], but it remains unclear whether the BCAS-mediated ChP immune inflammatory response involves NF-κB activation. Our study shows that BCAS induces phosphorylation activation of NF-κB, reflected by increased pNF-κB expression. Administration of SPAK protein inhibitor ZT-1a in the BCAS mice also reduced the expression of pNF-κB in the ChP. Interestingly, it has been reported that there is significant reduction of pNF-κB in renal tissues associated with IgA nephropathy in SPAK knockout mice [50]. These results collectively suggest a possible crosstalk between SPAK and NF-κB in different signaling pathways. The underlying mechanisms are not clear. Future studies are warranted to investigate signaling pathways in ZT-1a-mediated suppression of NF-κB phosphorylation and a possibility of inhibiting other kinase activities, as previously reported in vitro enzymatic assays [19].

SPAK inhibitor ZT-1a attenuates BCAS-induced neurological function deficit

In testing impact of ZT-1a treatment on neurological function impairment after BCAS, we conducted OF test and Y-maze test. OF test is employed to analyze locomotor behavior and anxiety states in rodents, with changes in behavior or locomotion potentially indicating changes in neural processes, and thus reflecting dysfunction in brain. Total distance traveled was used to assess the exploratory behavior and activity inclination of mice, and the number of vertical activities was used to assess exploratory behavior and curiosity [30, 51]. The BCAS + Veh group at 4-weeks post-BCAS exhibited a significant reduction in both total travel distance and vertical activities compared to the sham group, revealing a decrease in locomotor activity and exploratory drive following BCAS. However, the BCAS + ZT-1a group displayed no differences from the sham group. These findings suggest that the symptoms of reduced exploratory desire and activity inclination caused by BCAS can be effectively improved by the SPAK inhibitor ZT-1a. In the Y-maze test evaluating spatial working memory changes in these mice, there were no significant differences among the three groups (Sham, BCAS, BCAS + ZT-1a) in total arm entries or spontaneous alternation rates, indicating no impairment in spatial short-term memory function in the 4 weeks post-BCAS mice. But, significant deficits in spontaneous alternation and recognition index were detected in the 8-weeks BCAS + Veh mice. Therefore, 30-d post-BCAS is too early to detect the cognitive deficit in our current study. We reported recently that SPAK-NKCC1 complex is involved in white matter damage and astrogliosis in hippocampus and corpus collosum after BCAS and administration of SPAK inhibitor ZT-1a attenuated injury in these areas [52, 53]. Therefore, improved neurological function recovery by blocking SPAK-NKCC1 complex with ZT-1a likely result from collective protection of all brain regions.

Sex differences in cerebral blood flow regulation and effects of ZT-1a

Following BCAS surgery, male and female mice displayed different responses in changes in the CBF. Cardiovascular differences likely have a role in this disparity, as the cardiovascular risk for vascular dementia and the risk for severe cardiovascular events, such as heart attacks, are higher in human males [54]. However, if diagnosed, females are more likely to have more severe cases of vascular dementia, perhaps due to reduced estradiol levels, a potential neuro-protectant, in post-menopause females [27]. Sex differences in responses to CBF regulation in the BCAS model and its impact on cognitive function deficit development warrant further study.

Discrepancy in immunostaining and immunoblotting data

The causes for the discrepancy in immunostaining and immunoblotting data are not well understood. It could be due to regional hypoxic damage in the ChP in the LVCP resulting from different blood supply from the anterior choroidal artery (a branch of the internal carotid artery arising from the common carotid artery) and the posterior choroidal arteries, which are small branches of the

posterior cerebral artery arising from the basilar artery and aorta [55–57]. The BCAS model primarily affects blood flow in the common carotid arteries, which provide the partial blood supply to LVCP via the anterior choroidal artery. Presumably, the posterior choroidal arteries are not affected in the BCAS model, which likely contributes to non-homogenous reduction in CBF in different segments of the LVCP. Since the anterior choroidal artery enters the plexus at the end of the inferior cornu of the lateral ventricle [57], to maintain consistency in assessing the LVCP segment primarily supplied by the internal carotid artery in immunofluorescence staining experiments, brain sections (located between −0.5 and −1.0 mm from bregma, the 5th to 25th sections after the appearance of the LVCP) were selected. However, the Western blot data were from the entire LVCP tissues, including the LVCP region with the blood supply from both anterior choroidal artery and posterior choroidal arteries. This may explain that phenotype changes in specific sections of the LVCP are only detected by immunofluorescence staining assay but not with immunoblotting of the entire LVCP samples. Further research is warranted with improved approaches with higher detection sensitivity or pooled LVCP samples to separate cellular cytosol, membrane and nuclear fractions.

Conclusion

Considering various functions of ChP in the brain, damage of ChP and loss of the blood-CSF barrier are associated with many neurological disorders, leading to questions about its role in VCID. Here we report that BCAS model-induced chronic cerebral hypoperfusion leads to structural changes in the ChP, including elevation and dislocation of TJ proteins claudin-1 and claudin-5 expression, regional upregulation of the CSF secretory ionic regulatory proteins SPAK-NKCC1, and local activation of the NF-κB cascade, but absence of increased permeability to albumin. These changes are undone by the SPAK inhibitor ZT-1a treatment, accompanied by reduced influx of inflammatory immune cells in the ChP and cerebral hemisphere tissues. These results serve as structural and functional evidence for ChP damage following cerebral hypoperfusion. This research provides insights in chronic cerebral hypoperfusion-induced blood-CSF barrier damage and neuroinflammation in VCID.

Abbreviations

AD	Alzheimer's disease
ANOVA	One-way analysis of variance
ARRIVE	Animal Research Reporting In Vivo Experiments
BCA	Bicinchoninic acid assay
BCAS	Bilateral carotid artery coil stenosis
CBF	Cerebral blood flow
CCA	Common carotid artery
ChP	Choroid plexus
CNS	Central nervous system
CSF	Cerebrospinal fluid
Ctrl	Control
DMSO	Dimethyl sulfoxide
FBS	Fetal bovine serum
i.p.	Intraperitoneal injection
IFN-γ	Interferon gamma
IL-1	Interleukin-1β
IL-6	Interleukin-6
IκBα/β/ε	Inhibitory factor-KB proteins
IκK	The IκB kinase
LVCP	Lateral ventricle ChP
MMP-3	Matrix metalloproteinase 3
MMP-9	Matrix metalloproteinase 9
NF-κB	Nuclear factor kappa-light-chain-enhancer of activated B cells
NGS	Normal goat serum
NKCC1	Na+-K+-Cl−cotransporter isoform 1
OF	Open field
OSR1	Oxidative stress-responsive kinase-1
PBS	Phosphate Buffered Saline
pNKCC1	Phosphorylated NKCC1
pSPAK	Phosphorylated SPAK
rCBF	Regional CBF
ROIs	Regions of interest
RT	Room temperature
SD	Standard deviation
SPAK	Serine-proline-alanine kinase
TJ	Tight junctions
tMCAO	Transient middle cerebral artery occlusion
TNF-α	Tumor necrosis factor-alpha
Veh	Vehicle
WMLs	White matter lesions
Y-maze	Y-maze spontaneous alternation test
ZO-1	Zonula occludens protein 1

Supplementary Information

The online version contains supplementary material available at https://doi.org/10.1186/s12974-024-03209-1.

Additional file 1

Availability of data and material

Supporting data and information about used material are available from the corresponding author on request.

Declarations

Ethics approval and consent to participate

All animal experiments were conducted at the University of Pittsburgh and were approved by the University of Pittsburgh Medical Center Institutional Animal Care and Use Committee (IACUC), which adhere to the National Institutes of Health Guide for the Care and Use of Laboratory Animals.

Lin *et al. Journal of Neuroinflammation*   (2024) 21:220

Page 22 of 23

References

1. Ying C, Kang P, Binkley MM, Ford AL, Chen Y, Hassenstab J, et al. Neuroinflammation and amyloid deposition in the progression of mixed Alzheimer and vascular dementia. Neuroimage Clin. 2023;38: 103373.
2. Gladman JT, Corriveau RA, Debette S, Dichgans M, Greenberg SM, Sachdev PS, et al. Vascular contributions to cognitive impairment and dementia: research consortia that focus on etiology and treatable targets to lessen the burden of dementia worldwide. Alzheimers Dement (N Y). 2019;5:789–96.
3. Poliakova T, Wellington CL. Roles of peripheral lipoproteins and cholesteryl ester transfer protein in the vascular contributions to cognitive impairment and dementia. Mol Neurodegener. 2023;18(1):86.
4. Chen X, Chen L, Lin G, Wang Z, Kodali MC, Li M, et al. White matter damage as a consequence of vascular dysfunction in a spontaneous mouse model of chronic mild chronic hypoperfusion with eNOS deficiency. Mol Psychiatry. 2022;27(11):4754–69.
5. Custodero C, Ciavarella A, Panza F, Gnocchi D, Lenato GM, Lee J, et al. Role of inflammatory markers in the diagnosis of vascular contributions to cognitive impairment and dementia: a systematic review and meta-analysis. Geroscience. 2022;44(3):1373–92.
6. Rosenberg GA. Extracellular matrix inflammation in vascular cognitive impairment and dementia. Clin Sci (Lond). 2017;131(6):425–37.
7. Rodríguez-Lorenzo S, Ferreira Francisco DM, Vos R, van Het Hof B, Rijnsburger M, Schroten H, et al. Altered secretory and neuroprotective function of the choroid plexus in progressive multiple sclerosis. Acta Neuropathol Commun. 2020;8(1):35.
8. Strominger I, Elyahu Y, Berner O, Reckhow J, Mittal K, Nemirovsky A, et al. The choroid plexus functions as a niche for T-cell stimulation within the central nervous system. Front Immunol. 2018;9:1066.
9. Müller J, Sinnecker T, Wendebourg MJ, Schläger R, Kuhle J, Schädelin S, et al. Choroid plexus volume in multiple sclerosis vs neuromyelitis optica spectrum disorder: a retrospective, cross-sectional analysis. Neurol Neuroimmunol Neuroinflamm. 2022;9(3).
10. Kant S, Stopa EG, Johanson CE, Baird A, Silverberg GD. Choroid plexus genes for CSF production and brain homeostasis are altered in Alzheimer's disease. Fluids Barriers CNS. 2018;15(1):34.
11. Brkic M, Balusu S, Van Wonterghem E, Gorlé N, Benilova I, Kremer A, et al. Amyloid β oligomers disrupt blood-CSF barrier integrity by activating matrix metalloproteinases. J Neurosci. 2015;35(37):12766–78.
12. Robert SM, Reeves BC, Kiziltug E, Duy PQ, Karimy JK, Mansuri MS, et al. The choroid plexus links innate immunity to CSF dysregulation in hydrocephalus. Cell. 2023;186(4):764-85.e21.
13. Karimy JK, Zhang J, Kurland DB, Theriault BC, Duran D, Stokum JA, et al. Inflammation-dependent cerebrospinal fluid hypersecretion by the choroid plexus epithelium in posthemorrhagic hydrocephalus. Nat Med. 2017;23(8):997–1003.
14. Sadegh C, Xu H, Sutin J, Fatou B, Gupta S, Pragana A, et al. Choroid plexus-targeted NKCC1 overexpression to treat post-hemorrhagic hydrocephalus. Neuron. 2023;111(10):1591-608.e4.
15. Wang J, Liu R, Hasan MN, Fischer S, Chen Y, Como M, et al. Role of SPAK-NKCC1 signaling cascade in the choroid plexus blood-CSF barrier damage after stroke. J Neuroinflammation. 2022;19(1):91.
16. Li L, He G, Shi M, Zhu J, Cheng Y, Chen Y, et al. Edaravone dexborneol ameliorates cognitive impairment by regulating the NF-κB pathway through AHR and promoting microglial polarization towards the M2 phenotype in mice with bilateral carotid artery stenosis (BCAS). Eur J Pharmacol. 2023;957: 176036.
17. Nakano-Kobayashi A, Canela A, Yoshihara T, Hagiwara M. Astrocyte-targeting therapy rescues cognitive impairment caused by neuroinflammation via the Nrf2 pathway. Proc Natl Acad Sci U S A. 2023;120(33): e2303809120.
18. Bhuiyan MIH, Young CB, Jahan I, Hasan MN, Fischer S, Meor Azlan NF, et al. NF-κB signaling-mediated activation of WNK-SPAK-NKCC1 cascade in worsened stroke outcomes of Ang II-hypertensive mice. Stroke. 2022;53(5):1720–34.
19. Zhang J, Bhuiyan MIH, Zhang T, Karimy JK, Wu Z, Fiesler VM, et al. Modulation of brain cation-Cl(-) cotransport via the SPAK kinase inhibitor ZT-1a. Nat Commun. 2020;11(1):78.
20. Moriguchi T, Urushiyama S, Hisamoto N, Iemura S, Uchida S, Natsume T, et al. WNK1 regulates phosphorylation of cation-chloride-coupled cotransporters via the STE20-related kinases, SPAK and OSR1. J Biol Chem. 2005;280(52):42685–93.
21. Yang SS, Lo YF, Wu CC, Lin SW, Yeh CJ, Chu P, et al. SPAK-knockout mice manifest Gitelman syndrome and impaired vasoconstriction. J Am Soc Nephrol. 2010;21(11):1868–77.
22. Percie du Sert N, Hurst V, Ahluwalia A, Alam S, Avey MT, Baker M, et al. The ARRIVE guidelines 2.0: updated guidelines for reporting animal research. BMJ Open Sci. 2020;4(1):e100115.
23. Liu Q, Bhuiyan MIH, Liu R, Song S, Begum G, Young CB, et al. Attenuating vascular stenosis-induced astrogliosis preserves white matter integrity and cognitive function. J Neuroinflammation. 2021;18(1):187.
24. Gad SC, Cassidy CD, Aubert N, Spainhour B, Robbe H. Nonclinical vehicle use in studies by multiple routes in multiple species. Int J Toxicol. 2006;25(6):499–521.
25. Song S, Wang S, Pigott VM, Jiang T, Foley LM, Mishra A, et al. Selective role of Na(+) /H(+) exchanger in Cx3cr1(+) microglial activation, white matter demyelination, and post-stroke function recovery. Glia. 2018;66(11):2279–98.
26. Kunis G, Baruch K, Rosenzweig N, Kertser A, Miller O, Berkutzki T, et al. IFN-γ-dependent activation of the brain's choroid plexus for CNS immune surveillance and repair. Brain. 2013;136(Pt 11):3427–40.
27. Podcasy JL, Epperson CN. Considering sex and gender in Alzheimer disease and other dementias. Dialogues Clin Neurosci. 2016;18(4):437–46.
28. Lee EC, Hong DY, Lee DH, Park SW, Lee JY, Jeong JH, et al. Inflammation and rho-associated protein kinase-induced brain changes in vascular dementia. Biomedicines. 2022;10(2):446.
29. Kraeuter AK, Guest PC, Sarnyai Z. The open field test for measuring locomotor activity and anxiety-like behavior. Methods Mol Biol. 2019;1916:99–103.
30. Sukoff Rizzo SJ, Anderson LC, Green TL, McGarr T, Wells G, Winter SS. Assessing healthspan and lifespan measures in aging mice: optimization of testing protocols, replicability, and rater reliability. Curr Protoc Mouse Biol. 2018;8(2): e45.
31. Soria G, Tudela R, Márquez-Martín A, Camón L, Batalle D, Muñoz-Moreno E, et al. The ins and outs of the BCCAo model for chronic hypoperfusion: a multimodal and longitudinal MRI approach. PLoS ONE. 2013;8(9): e74631.
32. Bink DI, Ritz K, Aronica E, van der Weerd L, Daemen MJ. Mouse models to study the effect of cardiovascular risk factors on brain structure and cognition. J Cereb Blood Flow Metab. 2013;33(11):1666–84.
33. Nishio K, Ihara M, Yamasaki N, Kalaria RN, Maki T, Fujita Y, et al. A mouse model characterizing features of vascular dementia with hippocampal atrophy. Stroke. 2010;41(6):1278–84.
34. Washida K, Hattori Y, Ihara M. Animal models of chronic cerebral hypoperfusion: from mouse to primate. Int J Mol Sci. 2019;20(24):6176.
35. Gião T, Teixeira T, Almeida MR, Cardoso I. Choroid plexus in Alzheimer's disease-the current state of knowledge. Biomedicines. 2022;10(2):224.
36. Kratzer I, Ek J, Stolp H. The molecular anatomy and functions of the choroid plexus in healthy and diseased brain. Biochim Biophys Acta Biomembr. 2020;1862(11): 183430.
37. Municio C, Carrero L, Antequera D, Carro E. Choroid plexus aquaporins in CSF homeostasis and the glymphatic system: their relevance for Alzheimer's disease. Int J Mol Sci. 2023;24(1):878.
38. Weber CR, Nalle SC, Tretiakova M, Rubin DT, Turner JR. Claudin-1 and claudin-2 expression is elevated in inflammatory bowel disease and may contribute to early neoplastic transformation. Lab Invest. 2008;88(10):1110–20.

Lin *et al. Journal of Neuroinflammation*   (2024) 21:220

Page 23 of 23

39. Oshitani N, Watanabe K, Nakamura S, Fujiwara Y, Higuchi K, Arakawa T. Dislocation of tight junction proteins without F-actin disruption in inactive Crohn's disease. Int J Mol Med. 2005;15(3):407–10.
40. Chelakkot C, Ghim J, Ryu SH. Mechanisms regulating intestinal barrier integrity and its pathological implications. Exp Mol Med. 2018;50(8):1–9.
41. Cui J, Shipley FB, Shannon ML, Alturkistani O, Dani N, Webb MD, et al. Inflammation of the embryonic choroid plexus barrier following maternal immune activation. Dev Cell. 2020;55(5):617-28.e6.
42. Ruytinx P, Proost P, Van Damme J, Struyf S. Chemokine-induced macrophage polarization in inflammatory conditions. Front Immunol. 2018;9:1930.
43. Yadav S, Dwivedi A, Tripathi A. Biology of macrophage fate decision: implication in inflammatory disorders. Cell Biol Int. 2022;46(10):1539–56.
44. Rayasam A, Faustino J, Lecuyer M, Vexler ZS. Neonatal stroke and TLR1/2 ligand recruit myeloid cells through the choroid plexus in a CX3CR1-CCR2- and context-specific manner. J Neurosci. 2020;40(19):3849–61.
45. Zheng L, Jia J, Chen Y, Liu R, Cao R, Duan M, et al. Pentoxifylline alleviates ischemic white matter injury through up-regulating Mertk-mediated myelin clearance. J Neuroinflammation. 2022;19(1):128.
46. Wang Y, Wu Q, Fang Y, Song G, Xu L, Wang W, et al. Depletion of regulatory T cells exacerbates inflammatory responses after chronic cerebral hypoperfusion in mice. Mol Cell Neurosci. 2022;123: 103788.
47. Delpire E, Gagnon KB. Na(+) -K(+) -2Cl(-) cotransporter (NKCC) physiological function in nonpolarized cells and transporting epithelia. Compr Physiol. 2018;8(2):871–901.
48. Alvarez-Leefmans FJ. CrossTalk proposal: apical NKCC1 of choroid plexus epithelial cells works in the net inward flux mode under basal conditions, maintaining intracellular Cl(-) and cell volume. J Physiol. 2020;598(21):4733–6.
49. Johnsen L, Friis KA, Damkier HH. In vitro investigation of the effect of proinflammatory cytokines on mouse choroid plexus membrane transporters Ncbe and NKCC1. Fluids Barriers CNS. 2023;20(1):71.
50. Cao Q, Chen J, Zhang Z, Shu S, Qian Y, Yang L, et al. Astrocytic CXCL5 hinders microglial phagocytosis of myelin debris and aggravates white matter injury in chronic cerebral ischemia. J Neuroinflammation. 2023;20(1):105.
51. Whyte LS, Hemsley KM, Lau AA, Hassiotis S, Saito T, Saido TC, et al. Reduction in open field activity in the absence of memory deficits in the App(NL-G-F) knock-in mouse model of Alzheimer's disease. Behav Brain Res. 2018;336:177–81.
52. Bhuiyan MIH, Habib K, Sultan MT, Chen F, Jahan I, Weng Z, et al. SPAK inhibitor ZT-1a attenuates reactive astrogliosis and oligodendrocyte degeneration in a mouse model of vascular dementia. CNS Neurosci Ther. 2024;30(3): e14654.
53. Habib K, Sultan M, Jahan I, Rahman M, Sun D, Cao G, Bhuiyan MIH. SPAK Kinase Inhibitor ZT-1a Prevents Reactive Astrogliosis, Blood-Brain Barrier Breakdown, and Demyelination in a Mouse Model of VCID. 2024 International Stroke Conference Abstract, Stroke 55 (Suppl 1), ATP17-ATP17.
54. Akhter F, Persaud A, Zaokari Y, Zhao Z, Zhu D. Vascular dementia and underlying sex differences. Front Aging Neurosci. 2021;13: 720715.
55. Takahashi S, Suga T, Kawata Y, Sakamoto K. Anterior choroidal artery: angiographic analysis of variations and anomalies. AJNR Am J Neuroradiol. 1990;11(4):719–29.
56. Slater LA, Hoffman C, Drake J, Krings T. Pre-operative embolization of a choroid plexus carcinoma: review of the vascular anatomy. Childs Nerv Syst. 2016;32(3):541–5.
57. Gonzalez-Marrero I, Hernández-Abad LG, Castañeyra-Ruiz L, Carmona-Calero EM, Castañeyra-Perdomo A. Changes in the choroid plexuses and brain barriers associated with high blood pressure and ageing. Neurologia (Engl Ed). 2022;37(5):371–82.

Publisher's Note

Springer Nature remains neutral with regard to jurisdictional claims in published maps and institutional affiliations.